mathematics

MDPI

Article

Digital Fracture Surface Morphology and Statistical Characteristics of Granite Brazilian Tests after Non-Steady-State Thermal Disturbance

Yongjun Chen [1,2] and Tubing Yin [1,*]

[1] School of Resources and Safety Engineering, Central South University, Changsha 410083, China; yongjunc@outlook.com
[2] Department of Civil Engineering, Monash University, 3800 Melbourne, Australia
* Correspondence: tubing_yin@mail.csu.edu.cn

Abstract: With the widespread advent of digital technologies, traditional perspectives in rock mechanics research are poised for further expansion. This paper presents a Brazilian test conducted on granite after non-steady-state thermal disturbance at 25 °C, 200 °C, 400 °C, and 600 °C, with detailed documentation of the damage process and failure response using an acoustic emission (AE) apparatus and a digital image correlation (DIC) system. Subsequently, utilizing point cloud data captured by a three-dimensional (3D) laser scanning system, a digital reconstruction of the failed specimen's fracture surface was accomplished. The 3D fractal characteristics and roughness response of the digitized fracture surface were studied using the box-counting method and least squares approach. Furthermore, texture information of the digitized fracture surface was calculated using the Gray Level Co-occurrence Matrix (GLCM), and statistical characteristics describing the elevation distribution were analyzed. The results elucidate the influence of thermal disturbance temperature on the mechanical parameters of the specimen, acoustic emission behavior, surface strain field evolution, and digital fracture morphology characteristics. The findings indicate a non-linear degradation effect of temperature on the specimen's tensile strength, with a reduction reaching 80.95% at 600 °C, where acoustic emission activity also peaked. The rising thermal disturbance temperature inhibited the crack initiation load at the specimen's center but expanded the high-strain concentration areas and the growth rate of horizontal displacement. Additionally, varying degrees of linear or non-linear relationships were discovered between thermal disturbance temperature and the 3D fractal dimension of the fracture surface, average roughness (R_a), peak roughness (R_z), and root mean square roughness (R_q), confirming the potential of Rsm in predicting the 3D fractal dimension of Brazilian test fracture surfaces. The study of the GLCM of the digitized 3D fracture surface demonstrated a high dependency of its four second-order statistical measures on thermal disturbance temperature. Finally, the statistical parameters of the fracture surface's elevation values showed a significant non-linear relationship with thermal disturbance temperature, with a critical temperature point likely existing between 400 and 600 °C that could precipitate a sudden change in the fracture surface's elevation characteristics.

Keywords: granite; temperature; DIC; 3D digital reconstruction; GLCM

MSC: 28A80; 62J02; 62J05; 62-08; 68U01; 68U10

check for updates

Citation: Chen, Y.; Yin, T. Digital Fracture Surface Morphology and Statistical Characteristics of Granite Brazilian Tests after Non-Steady-State Thermal Disturbance. *Mathematics* **2024**, *12*, 670. https://doi.org/10.3390/math12050670

Academic Editor: Andrey Jivkov

Received: 30 January 2024
Revised: 17 February 2024
Accepted: 23 February 2024
Published: 24 February 2024

Copyright: © 2024 by the authors. Licensee MDPI, Basel, Switzerland. This article is an open access article distributed under the terms and conditions of the Creative Commons Attribution (CC BY) license (https://creativecommons.org/licenses/by/4.0/).

1. Introduction

As the global climate agenda intensifies, the dispute over the harmony between energy and environmental security continues to emerge. Against this backdrop, human demands for energy acquisition and the development of engineering environments are becoming increasingly stringent. High temperatures have become an unavoidable topic in recent years within the fields of energy and rock engineering. The development of deep-earth rock

engineering [1], including geothermal energy extraction [2–4], nuclear waste disposal [5,6], and underground energy storage [7,8], involves extensive thermal disturbances in rock masses. Research attention is now being directed towards these areas.

Granite has long been renowned for its high density and strength. Under thermal stress, its physical properties such as mass, volume, longitudinal wave velocity, elastic modulus, porosity, permeability, thermal conductivity, and acoustic emissions undergo changes [9–12]. These alterations are primarily attributed to significant changes in the internal rock water content, mineral composition, and skeletal structure [10,13]. In numerous instances, the structure of rock plays a dominant role, and reports by Lakirouhani et al. [14] also indicate that grain size, as one of the intrinsic structural characteristics of rocks, plays a significant role in the compressive and tensile properties of rock. As a quasi-brittle rock, granite's tensile strength is much lower than its compressive strength. Its thermal damage threshold temperature has been proven to be approximately 400 °C. Furthermore, tensile failure is generally the main form of failure in engineered granite rock masses, making the tensile properties of granite particularly crucial for high-temperature rock engineering. Although the tensile strength obtained by the Brazilian test method may have certain deviations compared to the direct tension method, it remains the primary method for testing rock tensile strength at this stage. Zhi et al. [15] studied the tensile strength of granite subjected to temperature treatment up to 1000 °C, finding significant temperature-induced degradation and a certain degree of correlation between P-wave velocity and tensile strength. On the other hand, Wu et al. [16] further explored the physico-mechanical properties and acoustic emission characteristics of granite after high-temperature treatment through Brazilian split tests. Their results indicated that the tensile strength of granite gradually decreases with increasing temperature, with its thermal damage threshold temperature lying between 400 and 600 °C. Regrettably, research on the fracture surfaces of rocks post-Brazilian tests remains scarcely reported.

As research progresses, the traditional thermal disturbance model has shifted its focus towards the transient modes in actual engineering projects, as damage caused by temperature gradients in extreme environments is significantly more severe than that caused by traditional steady-state thermal disturbances. To generate larger temperature gradients, more aggressive cooling methods are employed, typically including air cooling, water cooling, and low-temperature media cooling such as liquid nitrogen [17]. Jin et al. [18] studied granite using heating and water cooling treatments, determining that its brittle-ductile transition temperature range is between 500 and 600 °C. Wang et al. [19] investigated the tensile strength of granite after high-temperature natural cooling and water cooling treatments, finding that water cooling leads to more severe damage in granite's tensile strength, with 200 °C being the threshold temperature for significant damage after high-temperature water cooling treatment. Ge et al. [20] examined the effects of liquid nitrogen cooling on the tensile fracture behavior of granite after high temperatures, concluding that 400 °C is the critical temperature threshold for the transition from brittleness to toughness in granite. Li et al. [21] utilized the discrete element method to simulate thermal shock in granite caused by rapid thermal changes, discovering that thermal shock-induced stress concentration promotes the coalescence of pre-existing heating cracks.

The rapid advancement of 3D printing technology, combined with highly sensitive and high-resolution image capture devices, has enabled near non-destructive and highly accurate digital 3D reconstruction of objects. The integration of this technology with editable processing algorithms has opened new research directions for in-depth understanding of material fracture information [22–24]. Particularly, point cloud data collection techniques, exemplified by mobile 3D laser scanning, have been proven to be precise, convenient, and high-resolution methods for digital reconstruction [25,26].

Traditionally, the study of rock joint surface characteristics has primarily relied on empirical and classic statistical methods, extensively using parameters such as slope angle, horizontal direction, height difference, curvature, and the Joint Roughness Coefficient (JRC) to describe the morphology of rock surfaces [27–30]. Although the roughness of 3D

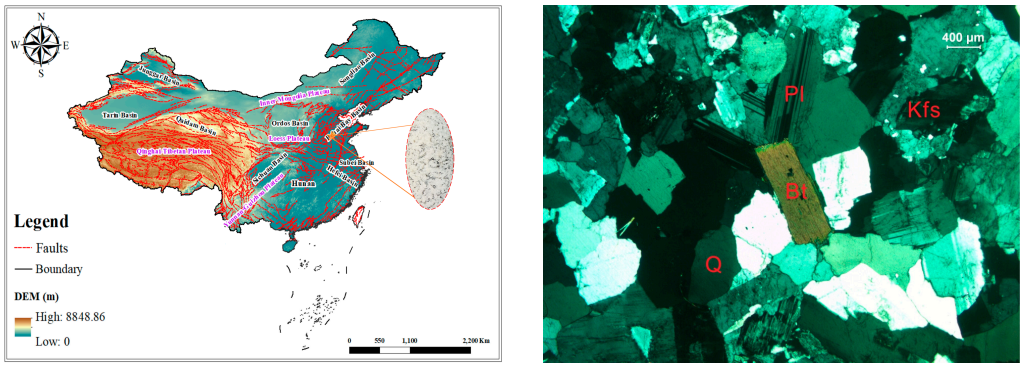
surfaces cannot be defined within the traditional Euclidean geometric system, they still exhibit significant fractal characteristics [31,32]. With the advancement of three-dimensional imaging technology, the theory and computational methods for fractal dimensions on a three-dimensional scale have also been well developed [33,34]. For example, Yin et al. [35] digitally reconstructed the Type I fracture surface of granite subjected to cyclic thermal shock using 3D laser scanning technology. Based on the point cloud data, they calculated its fractal dimension. Their results indicated a positive correlation between temperature and cycle number with fractal dimension, and a negative correlation with the brittleness index. Chen et al. [36] used 3D laser technology to study the image characteristics of fracture surfaces in cracked rocks after high-temperature cyclic impact failure. They found that the fractal dimension, roughness characterization factor, and JRC of fracture surfaces exhibit specific response patterns to temperature and crack angles.

Considering that in actual high-temperature engineering environments, the degradation of non-steady-state thermally disturbed rock masses is predominantly characterized by tensile failure, this paper utilizes AE and DIC systems to monitor the damage and failure strain evolution of granite in Brazilian tests after non-steady-state thermal disturbance, with thermal disturbance temperatures of 25, 200, 400, and 600 °C. The fracture surfaces are digitally reconstructed using three-dimensional laser scanning technology, and the fractal and roughness characteristics of the fracture surfaces are described combining the box-counting method and the least squares method. Furthermore, this study meticulously characterized the texture features of digital images of digitized three-dimensional fracture surfaces using the GLCM method. It also analyzed the response patterns of a series of statistical parameters based on elevation features.

2. Materials and Methods

2.1. Material Features and Sample Preparation

The granite samples for this study were collected from the Jining area of North China, as shown in Figure 1a. The rock exhibits a typical fine-grained granitic texture and massive structure. There is only minor kaolinization of potassium feldspar and weak biotitization of biotite. The composition mainly consists of potassium feldspar (40%), quartz (35%), plagioclase (20%), biotite (4%), with trace amounts of chlorite, apatite, zircon, and opaque minerals (1%), characterizing it as a typical fine-grained biotite granite, as depicted in Figure 1b.



(**a**) (**b**)

Figure 1. Geological characteristics of samples: (**a**) geological profile information; (**b**) optical microscopic slices of granite.

Subsequently, the collected granite samples were processed into cylindrical forms with a diameter of 50 mm and a height of 25 mm, in accordance with the recommended standards of the International Society for Rock Mechanics (ISRM) [37]. This process ensured that the non-parallelism of the sample surfaces was less than 0.02 mm and that the end surfaces

perpendicular to the axis were under 0.001 rad. The fundamental physical parameters of the granite are also presented in Table 1.

Table 1. Basic physical and mechanical parameters of the granite.

Type	Density, ρ (g/cm^3)	P-Wave Velocity, V_P (m/s)	Elastic Modulus, E (GPa)	Poisson's Ratio, μ	Compressive Strength (MPa)
Granite	2.6	3054.85	21.73	0.24	156.27

2.2. Thermal Treatments

Furthermore, to replicate the non-steady-state high-temperature disturbances encountered by engineering rock masses in actual engineering environments as closely as possible within the instrumental functional accuracy, four thermal treatment levels were selected as grouping criteria: 25, 200, 400, and 600 °C. The basic physical parameters of the specimens prepared for heat treatment are given in Table 2. Subsequently, the thermal treatment of samples at each temperature level was conducted in a rapid-heating muffle furnace equipped with a thermocouple-containing electronic temperature control device. The equipment's maximum temperature capability is 1200 °C. To generate an effective temperature gradient, the heating rate was set at 0.3 °C/s, which represents the maximum effective heating efficiency monitored by the muffle furnace. Once the temperature of the sample reached the predetermined target, it was immediately removed and cooled in a cold air stream at approximately 15 °C until no further decrease in the sample temperature was observed.

Table 2. The basic physical parameters of granite samples before heat treatment.

T (°C)	D (mm)	L (mm)	ρ (g/cm^3)	V_P (m/s)
25	49.35	24.91	2.58	2983.23
	50.04	24.77	2.60	3058.02
	50.04	25.11	2.53	3043.64
200	49.99	24.97	2.60	3030.34
	49.51	25.04	2.59	3083.74
	49.16	24.99	2.60	3245.45
400	49.71	24.92	2.60	3057.67
	49.39	24.89	2.58	3170.70
	49.43	24.9	2.60	3055.21
600	49.23	24.98	2.60	3223.23
	49.51	24.95	2.58	3223.51
	49.42	24.84	2.60	3044.12

2.3. Testing Setup and Scheme

The post-thermal disturbance samples undergo a testing program comprising three parts, as depicted in Figure 2. In the first part, an AE testing apparatus and a digital image correlation (DIC) system are utilized to capture the acoustic emission events and the evolution of the planar strain field during the Brazilian test conducted on an INSTRON 1342 testing machine. The second part involves the digital 3D imaging of the fractured surfaces of the Brazilian split specimens, specifically through the reconstruction of the digital fracture surfaces using a handheld 3D laser scanning system, followed by point cloud processing. In the third part, high-precision point cloud data are used for the digital characterization of the fracture surface morphology, further employing digital image techniques and statistical methods to delineate the fracture surfaces.



Figure 2. Schematic diagram of the experimental procedure and apparatus.

2.4. The Digital Image Correlation Method

DIC technology is a non-contact, real-time, and flexible optical method used for measuring the shape, displacement, and strain of objects. The essence of this technology lies in monitoring and tracking minute changes on the surface of an object by analyzing a sequence of images [38]. Presently, this technology has been widely applied in the fields of rock mechanics and materials mechanics [39,40]. It is important to note that the precision of parameters obtained through DIC technology primarily depends on factors such as the clarity of the captured images, the selection and distribution of measurement points, algorithm performance, the camera and optical system, and software post-processing [41].

In DIC testing, particular attention is focused on the following steps to ensure the accuracy and reliability of the measurements as much as possible [38,42,43]. On the surface of the specimen, a white matte background and black clear matte measurement speckles are successively added using a dye, ensuring a dry, grease-free, and non-reflective surface. These speckle points should be as randomly distributed as possible to avoid algorithmic misinterpretation, while ensuring that the size and contrast of the speckles match the camera and specimen size without compromising accuracy; typically, each speckle should cover at least 3–5 pixels. Ideally, speckles should cover 60% to 80% of the test area. Such coverage ensures sufficient randomness while avoiding overly dense speckle patterns.

After capturing the entire deformation process of the specimen recorded by the camera, these images are used as inputs for the DIC program. The first image, as the initial image, serves as the reference frame, and the subsequent images as deformation calculation images. This approach aims to establish a one-to-one correspondence between material points in the reference (initial undeformed image) and current (subsequent deformed image) configurations. Subsequently, the ROI is divided into multiple subsets, and displacement and strain information is obtained through transformation to match the position of the subsets in the current configuration. Many subsets are selected in the reference configuration, often setting a spacing parameter to reduce computational costs. The final result is a grid containing displacement and strain information relative to the reference configuration, also known as Lagrangian displacement/strain. Then, the displacement/strain field can be downscaled or interpolated to form a "continuous" displacement/strain field. The focus is on establishing a measure of similarity between the final reference subset and the final current subset by comparing the grayscale values at the final reference subset points

with those at the final current subset points. Two metrics commonly used in DIC are as follows [44]:

$$C_{cc} = \frac{\sum_{(i,j)\in s}\left(f\left(\tilde{x}_{ref_i},\tilde{y}_{ref_j}\right)-f_m\right)\left(g\left(\tilde{x}_{cur_i},\tilde{y}_{cur_j}\right)-g_m\right)}{\sqrt{\sum_{(i,j)\in s}\left[f\left(\tilde{x}_{ref_i^i},\tilde{y}_{ref_j}\right)-f_m\right]^2\sum_{(i,j)\in s}\left[g\left(\tilde{x}_{cur_i},\tilde{y}_{cur_j}\right)-g_m\right]^2}} \quad (1)$$

$$C_{LS} = \sum_{(i,j)\in s}\left[\frac{f\left(\tilde{x}_{ref_i},\tilde{y}_{ref_j}\right)-f_m}{\sqrt{\sum_{(i,j)\in s}\left[f\left(\tilde{x}_{ref_i},\tilde{y}_{ref_j}\right)-f_m\right]^2}}-\frac{g\left(\tilde{x}_{cur_i},\tilde{y}_{cur_j}\right)-g_m}{\sqrt{\sum_{(i,j)\in s}\left[g\left(\tilde{x}_{cur_i},\tilde{y}_{cur_j}\right)-g_m\right]^2}}\right]^2 \quad (2)$$

In the formulations above, $f\left(\tilde{x}_{ref_i},\tilde{y}_{ref_j}\right)$ and $g\left(\tilde{x}_{cur_i},\tilde{y}_{cur_j}\right)$ represent the reference image function and the current image function, respectively, returning the grayscale value corresponding to a specified point (x, y). fm and gm are the average grayscale values of the final reference and current subsets, respectively, and can be defined as follows:

$$f_m = \frac{\sum_{(i,j)\in s} f\left(\tilde{x}_{ref_i},\tilde{y}_{ref_j}\right)}{n(S)} \quad (3)$$

$$g_m = \frac{\sum_{(i,j)\in s} g\left(\tilde{x}_{cur_i},\tilde{y}_{cur_j}\right)}{n(S)} \quad (4)$$

In this context, $n(S)$ represents the number of elements within set S. Equation (1) defines the normalized cross-correlation criterion, indicating good matching when the C_{CC} approaches 1. Equation (2) represents the normalized least squares criterion, suggesting good matching as the C_{LS} approaches 0. Subtracting the average components (f_m and g_m) in Equations (1) and (2) allows the standard to remain invariant to changes in grayscale values, while division by the quantities in the denominator ensures invariance of the standard relative to scaled grayscale values. The final result is a correlation criterion that is invariant to affine displacements of grayscale values. Practically, each correlation standard is computationally more feasible under certain circumstances, and Figure 3 provides a simple illustration of these two criteria.

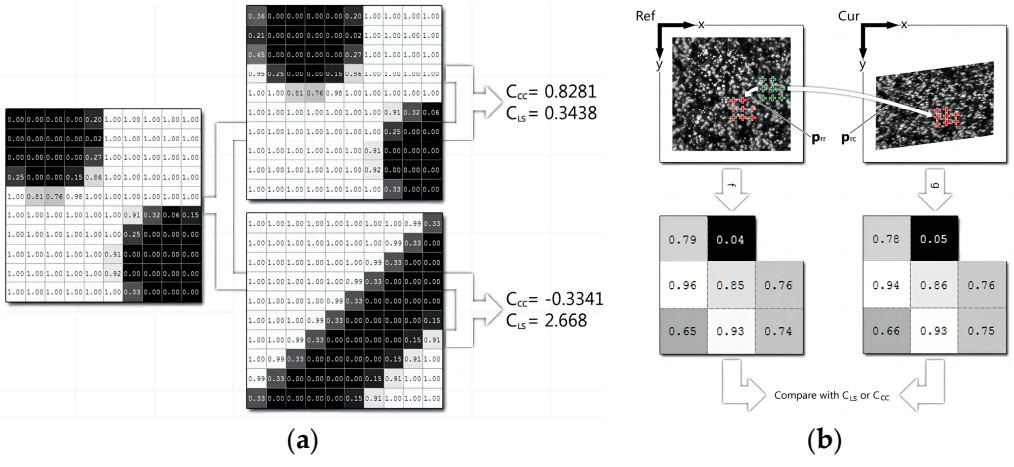
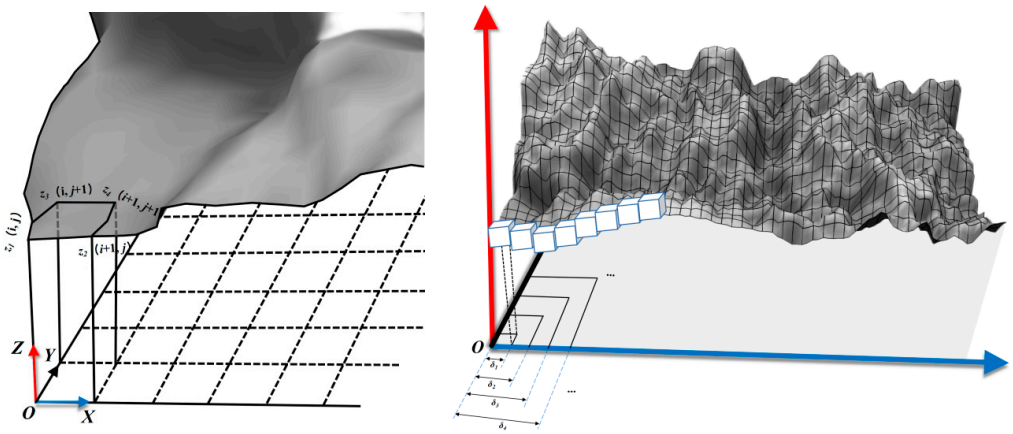


Figure 3. An example demonstrating the effectiveness of the two correlation criteria: (**a**) the grayscale value on the left is compared with two grayscale values on the right. The correlation criteria indicate that the grayscale value in the upper right matches the set of grayscale values on the left (C_{CC} close to 1, C_{LS} close to 0). (**b**) In the reference image, the green subset represents the initial reference subset, and the red subset marks the positions of the final subsets in both the reference and current configurations [44].

2.5. 3D Fractal and Roughness Characteristics of Fracture Surface

A substantial body of research and observational data has demonstrated that a considerable number of materials exhibit similarities in both macroscopic and microscopic morphological characteristics post-failure, such as fracture morphology, crack evolution paths, and dislocation distribution information. This similarity might suggest the existence of a universal system in the fracture and deformation of materials, and fractal dimensions can effectively unify and mathematically describe these deformation characteristics. Moreover, with the advancement of non-contact data acquisition technologies and computer science, employing fractal dimensions to characterize the three-dimensional contour features of rock fracture morphologies has become feasible. The most representative mathematical methods currently used for calculating fractal dimensions include the divider method, box-counting method, spectral or frequency methods, and other approaches such as variograms or semivariograms [35,45]. Compared to other methods, the box-counting method (also known as the cubical covering method) does not involve approximate calculations and is thus the most reliable in terms of computational accuracy. Consequently, this paper primarily employs the box-counting method for calculations. Similar to the principle of covering an irregular curve with fixed-side-length two-dimensional squares, the principle of the cubical covering method involves using fixed-side-length cubes to cover a three-dimensional surface with fractal characteristics. The specific principle is as follows:

Initially, the captured point cloud data of the three-dimensional rough surface are rendered and filtered to remove noise points. Subsequently, a digital elevation model, as shown in Figure 4, is established on the *XOY* plane. Assume the existence of a square grid with a side length of δ in the *XOY* coordinate system. The four corner points of the grid, (i, j), (i, j + 1), (i + 1, j), and (i + 1, j + 1), correspond to four points on the surface with heights $z_1(i, j)$, $z_2(i, j + 1)$, $z_3(i + 1, j)$, and $z_4(i + 1, j + 1)$, respectively (where $i \geq 1$, $j \leq n - 1$, and n is the number of measurement points per side).



(**a**) (**b**)

Figure 4. Procedures for determining the box-counting dimension of a fracture surface: (**a**) digital surface projection; (**b**) cubes with side length δ covering the fracture surface [33].

Consequently, the requisite quantity of cubes to envelop the entire surface is denoted by $N_{i,j}$, as can be inferred from these equations [46]:

$$N_{i,j} = \mathrm{INT}\left\{\delta^{-1}[\max(z_1(i,j), z_2(i+1,j), z_3(i,j+1), z_4(i+1,j+1)) - \min(z_1(i,j), z_2(i+1,j), z_3(i,j\pm1), z_4(i+1,j+1))] + 1\right\} \quad (5)$$

INT signifies the integral function. To envelop the entire fracture surface, the cumulative count of cubes is deduced as:

$$N(\delta) = \sum_{i,j=1}^{n-1} N_{i,j} \quad (6)$$

The association between $N(\delta)$ and δ, as per fractal theory, is articulated thus:

$$N(\delta) \sim \delta^{-Dc} \tag{7}$$

D_C represents the fractal dimension. The interrelation between $lnN(\delta)$ and $ln\delta$ emerges following a logarithmic alteration of Equation (8):

$$D_C = -\lim_{\delta \to 0} \frac{lnN_\delta(\Sigma)}{ln\delta} \tag{8}$$

Equation (8) elucidates that the fractal dimension, D_C, is governed by the quantity and dimensions of cubes necessary for encompassing the fracture surface Σ.

The three-dimensional roughness of rock fracture surfaces is of significant importance in the analysis of rock mechanics behavior and stability. For instance, in the determination of the mechanical properties of rocks, roughness measurements contribute to a more accurate assessment of mechanical properties such as the elastic modulus and Poisson's ratio, which are crucial for understanding the mechanical behavior of rocks. For example, in the analysis of rock mass structural stability, the roughness of rock fracture surfaces directly impacts the stability of the rock structure. Rock fracture surfaces with higher roughness typically possess desirable shear strength and frictional properties [47]. Furthermore, in studies of crack propagation and fracture mechanics, the complexity of crack propagation along rough surfaces necessitates a greater amount of energy to overcome the resistance caused by irregular surfaces. In this context, roughness serves as a key parameter [48].

Calculating the three-dimensional roughness of a section based on point cloud data involves several steps, including computations to extract surface characteristics from the point cloud data. Plane Fitting: Initially, the point cloud data is is used to fit a plane to the surface based on the method of least squares to obtain a reference plane. The objective of the least squares method is to minimize the sum of the squares of the vertical distances from each point to the plane. If the plane equation is given by $Ax + By + Cz + D = 0$, the optimal fitting condition is found by adjusting the coefficients A, B, C, and D. Distance Calculation: The vertical distance from each data point P(x, y, z) in the point cloud to the reference plane can be calculated using the following formula [49,50]:

$$d = \frac{|Ax + By + Cz + D|}{\sqrt{A^2 + B^2 + C^2}} \tag{9}$$

Herein, d represents the distance and can also be considered as the height of the surface. Based on these parameters, the roughness parameters that can typically be calculated are as follows [51–54]:

Average roughness (R_a) is the mean of the absolute values of all height values. The formula for calculation is:

$$R_a = \frac{1}{n}\sum_{i=1}^{n}|d_i| \tag{10}$$

where n is the total number of points in the point cloud, and d_i is the distance of the i^{th} point from the reference plane.

Peak-to-valley roughness (R_z) is the difference between the highest and lowest points. Its formula is:

$$R_z = \max(d_i) - \min(d_i) \tag{11}$$

Root mean square roughness (R_q) is the square root of the average of the squared height values. Its formula is:

$$R_q = \sqrt{\frac{1}{n}\sum_{i=1}^{n}{d_i}^2} \tag{12}$$

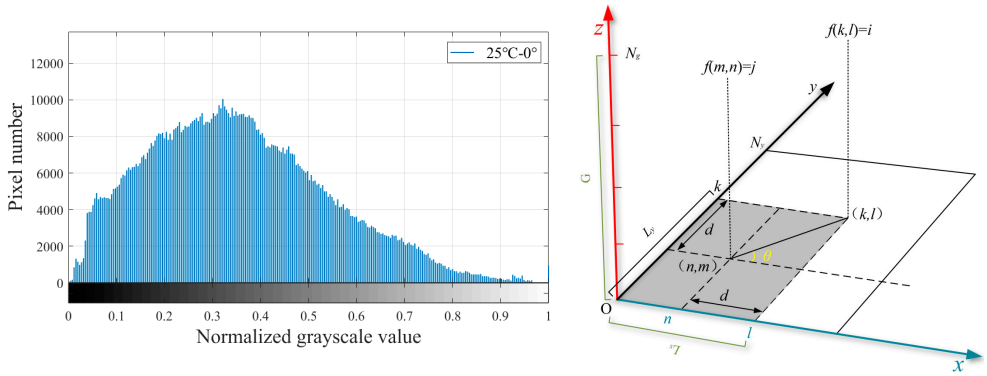
To calculate the average slope between every two adjacent points, if the coordinates of points P_i and P_{i+1} are (x_i, y_i, z_i) and $(x_{i+1}, y_{i+1}, z_{i+1})$, respectively, then the average peak-to-peak distance (R_{sm}) can be derived from the following formula:

$$R_{sm} = \frac{1}{n-1}\sum_{i=1}^{n}\frac{\sqrt{(x_{i+1}-x_i)^2+(y_{i+1}-y_i)^2+(z_{i+1}-z_i)^2}}{d_{i+1}-d_i} \tag{13}$$

2.6. The Gray Level Co-Occurrence Matrix

The GLCM method has been selected for analyzing the texture traits of DALC impact fracture surfaces, owing to its enhanced adaptability and reliability [55]. Texture in a grayscale image arises from repetitive patterns of grayscale values at specific spatial locations, creating a defined grayscale correlation between two pixels at a certain distance or orientation within the image space.

Consider Figure 5, where *XOY* represents the coordinate plane of the image pixels, and the *Z*-axis symbolizes the grayscale coordinate. The function f represents the relationship between the plane pixel dimensions $L_x \times L_y$ and the spatial grayscale intensity G. The total pixel counts in the x and y directions are denoted as N_x and N_y, respectively, with N_g being the highest gray level. The variable d signifies the separation between any two pixels, while θ indicates the angle formed between the line connecting these two pixels and the x-axis.



(**a**) (**b**)

Figure 5. (**a**) Pixel gray scale frequency histogram; (**b**) correspondence in the pixel plane coordinate system [33].

Consequently, a GLCM, considering pixel grayscale values, distances, and orientations, can be defined through the joint probability matrix $P_{\alpha,d(i,j)}$ in the following manner [56]:

$$\begin{cases} P(i,j,d,\theta) \\ D = (L_y \times L_x)(L_y \times L_x) \end{cases} \tag{14}$$

$$\begin{cases} P(i,j,d,0^\circ) = |\{[(k,l),(m,n)] \in D : k-m=0, |l-n|=d;\ f(k,l)=i,\ f(m,n)=j\}| \\ P(i,j,d,45^\circ) = |\{[(k,l),(m,n)] \in D : (k-m=d, l-n=-d)\ or\ (k-m=-d, l-n=d);\ f(k,l)=i, f(m,n)=j\}| \\ P(i,j,d,90^\circ) = |\{[(k,l),(m,n)] \in D : (|k-m|=d, l-n=0; f(k,l)=i,\ f(m,n)=j\}| \\ P(i,j,d,135^\circ) = |\{[(k,l),(m,n)] \in D : (k-m=d, l-n=d)\ or\ (k-m=-d, l-n=-d),\ f(k,l)=i, f(m,n)=j\}| \end{cases} \tag{15}$$

Herein, $|\{\cdots\}|$ refers to the cardinality of the set. To reduce computational load, this paper processes the acquired original images into grayscale and compresses the grayscale levels to 16. The computation of the rough cross-sectional images involves generating normalized GLCM at a distance d of 1, in directions of 0°, 45°, 90°, and 135°, as illustrated in Figure 6.

$P(0°,1)$ =

0.0034	0.0021	0	0	0	0	0	0	0	0	0	0	0	0	0	0
0.0021	0.0829	0.0057	0	0	0	0	0	0	0	0	0	0	0	0	0
0	0.0057	0.0599	0.0082	0	0	0	0	0	0	0	0	0	0	0	0
0	0	0.0082	0.0585	0.0096	0	0	0	0	0	0	0	0	0	0	0
0	0	0	0.0096	0.0650	0.0111	0	0	0	0	0	0	0	0	0	0
0	0	0	0	0.0111	0.0676	0.0113	0	0	0	0	0	0	0	0	0
0	0	0	0	0	0.0113	0.0641	0.0116	0	0	0	0	0	0	0	0
0	0	0	0	0	0	0.0116	0.0782	0.0120	0	0	0	0	0	0	0
0	0	0	0	0	0	0	0.0120	0.0729	0.0112	0	0	0	0	0	0
0	0	0	0	0	0	0	0	0.0112	0.0662	0.0092	0	0	0	0	0
0	0	0	0	0	0	0	0	0	0.0092	0.0562	0.0074	0	0	0	0
0	0	0	0	0	0	0	0	0	0	0.0074	0.0421	0.0043	0	0	0
0	0	0	0	0	0	0	0	0	0	0	0.0043	0.0299	0.0025	0	0
0	0	0	0	0	0	0	0	0	0	0	0	0.0025	0.0235	0.0016	0
0	0	0	0	0	0	0	0	0	0	0	0	0	0.0016	0.0083	0
0	0	0	0	0	0	0	0	0	0	0	0	0	0	0	0.0058

$P(45°,1)$ =

0.0028	0.0026	0.0001	0	0	0	0	0	0	0	0	0	0	0	0	0.0001
0.0026	0.0814	0.0068	0	0	0.0001	0	0	0	0	0	0	0	0	0	0.0001
0.0001	0.0068	0.0573	0.0095	0	0	0	0	0	0	0	0	0	0	0	0.0001
0	0	0.0095	0.0553	0.0112	0	0	0	0	0	0	0	0	0	0	0.0002
0	0	0	0.0112	0.0611	0.0133	0	0	0	0	0	0	0	0	0	0.0001
0	0.0001	0	0	0.0133	0.0610	0.0140	0.0002	0.0001	0.0001	0.0001	0.0001	0.0002	0	0	0.0010
0	0	0	0	0	0.0140	0.0582	0.0147	0.0001	0	0	0	0	0	0	0.0001
0	0	0	0	0	0.0002	0.0147	0.0719	0.0149	0.0001	0	0	0	0	0	0.0001
0	0	0	0	0	0.0001	0.0001	0.0149	0.0676	0.0134	0	0	0	0	0	0.0001
0	0	0	0	0	0.0001	0	0.0001	0.0134	0.0618	0.0112	0	0	0	0	0.0001
0	0	0	0	0	0.0001	0	0	0	0.0112	0.0523	0.0093	0	0	0	0
0	0	0	0	0	0.0001	0	0	0	0	0.0093	0.0386	0.0058	0	0.05	
0	0	0	0	0	0.0002	0	0	0	0	0	0.0058	0.0273	0.0032	0	0
0	0	0	0	0	0	0	0	0	0	0	0	0.0032	0.0226	0.0019	0
0	0	0	0	0	0	0	0	0	0	0	0	0	0.0019	0.0081	0
0.0001	0.0001	0.0001	0.0002	0.0001	0.0010	0.0001	0.0001	0.0001	0.0001	0	0	0	0	0	0.0019

$P(90°,1)$ =

0.0040	0.0013	0.0001	0	0	0	0	0	0	0	0	0	0	0	0	0.0001
0.0013	0.0856	0.0037	0	0	0.0001	0	0	0	0	0	0	0	0	0	0.0001
0.0001	0.0037	0.0643	0.0058	0	0	0	0	0	0	0	0	0	0	0	0.0001
0	0	0.0058	0.0633	0.0071	0	0	0	0	0	0	0	0	0	0	0.0002
0	0	0	0.0071	0.0701	0.0086	0	0	0	0	0	0	0	0	0	0.0001
0	0.0001	0	0	0.0086	0.0706	0.0092	0.0001	0.0001	0.0001	0.0001	0.0001	0.0002	0	0	0.0010
0	0	0	0	0	0.0092	0.0680	0.0097	0.0001	0	0	0	0	0	0	0.0001
0	0	0	0	0	0.0001	0.0097	0.0812	0.0105	0	0	0	0	0	0	0.0001
0	0	0	0	0	0.0001	0.0001	0.0105	0.0752	0.0099	0	0	0	0	0	0.0001
0	0	0	0	0	0.0001	0	0	0.0099	0.0681	0.0083	0	0	0	0	0.0001
0	0	0	0	0	0.0001	0	0	0	0.0083	0.0574	0.0071	0	0	0	0
0	0	0	0	0	0.0001	0	0	0	0	0.0071	0.0419	0.0047	0	0	0
0	0	0	0	0	0.0002	0	0	0	0	0	0.0047	0.0294	0.0025	0	0
0	0	0	0	0	0	0	0	0	0	0	0	0.0025	0.0244	0.0011	0
0	0	0	0	0	0	0	0	0	0	0	0	0	0.0011	0.0088	0
0.0001	0.0001	0.0001	0.0002	0.0001	0.0010	0.0001	0.0001	0.0001	0.0001	0	0	0	0	0.0000	0.0019

$P(135°,1)$ =

0.0027	0.0026	0.0001	0	0	0	0	0	0	0	0	0	0	0	0	0.0001
0.0026	0.0809	0.0072	0	0	0.0001	0	0	0	0	0	0	0	0	0	0.0001
0.0001	0.0072	0.0558	0.0106	0.0001	0	0	0	0	0	0	0	0	0	0	0.0011
0	0	0.0106	0.0528	0.0124	0.0002	0	0	0	0	0	0	0	0	0	0.0002
0	0	0.0001	0.0124	0.0587	0.0142	0.0003	0	0	0	0	0	0	0	0	0.0001
0	0.0001	0	0.0002	0.0142	0.0591	0.0147	0.0003	0.0001	0.0001	0.0001	0.0001	0.0002	0	0	0.0010
0	0	0	0	0.0003	0.0147	0.0565	0.0153	0.0002	0	0	0	0	0	0	0.001
0	0	0	0	0	0.0003	0.0153	0.0693	0.0166	0.0002	0	0	0	0	0	0.001
0	0	0	0	0	0.0001	0.0002	0.0166	0.0632	0.0158	0.0002	0	0	0	0	0.001
0	0	0	0	0	0.0001	0	0.0002	0.0158	0.0571	0.0132	0.0002	0	0	0	0.0001
0	0	0	0	0	0.0001	0	0	0.0002	0.0132	0.0485	0.0109	0.0001	0	0	0
0	0	0	0	0	0.0001	0	0	0	0.0002	0.0109	0.0357	0.0070	0	0	0
0	0	0	0	0	0.0002	0	0	0	0	0.0001	0.0070	0.0254	0.0039	0	0
0	0	0	0	0	0	0	0	0	0	0	0	0.0039	0.0216	0.0022	0
0	0	0	0	0	0	0	0	0	0	0	0	0	0.0022	0.0078	0
0.0001	0.0001	0.0001	0.0002	0.0001	0.0010	0.0001	0.0001	0.0001	0.0001	0	0	0	0	0	0.0019

Figure 6. Schematic diagram of the normalized grayscale co-occurrence matrix of rock fracture surface (d = 1, direction: 0 °, 45 °, 90 °, and 135 °).

Subsequent computations involve second-order statistical measures, such as angular second-order moments (*ASM*), entropy (*ENT*), contrast (*CON*), and correlation (*COR*) for each directional GLCM. In our notation, *P(r, c)* represents the elements of GLCM, with *r* and *c* designating the row and column elements of the matrix, respectively.

The *ASM* is generally smaller when there is a higher uniformity in the GLCM elements, and this relationship can be described as follows:

$$ASM = \sum_{r=0}^{L-1} \sum_{c=0}^{L-1} P\left(r,c\right)^2 \tag{16}$$

The *COR* illustrates the resemblance among adjacent pixels along both horizontal and vertical axes. The formula is articulated thus:

$$COR = \sum_{r=0}^{L-1} \sum_{c=0}^{L-1} \frac{rcP(r,c) - q_1 q_2}{t_1 t_2} \tag{17}$$

$$\begin{cases} q_1 = \sum_{c=0}^{L-1} c \sum_{r=0}^{L-1} P(c,r) \\ q_2 = \sum_{c=0}^{L-1} r \sum_{r=0}^{L-1} P(c,r) \\ t_1 = \sum_{c=0}^{L-1} (c-q_1)^2 \sum_{r=0}^{L-1} P(c,r) \\ t_2 = \sum_{c=0}^{L-1} (r-q_2)^2 \sum_{r=0}^{L-1} P(c,r) \end{cases} \quad (18)$$

The *ENT* reflects the intricacy of the image's texture, where a more scattered distribution of matrix elements leads to a lesser variance. This is computed as per the equation given below:

$$ENT = -\sum_{r=0}^{L-1} \sum_{c=0}^{L-1} P(r,c) lg P(r,c) \quad (19)$$

The *CON* represents the inertia around the principal diagonal within the GLCM, indicating the profundity and perceptual sharpness of the texture's gullies. Its computation is as follows:

$$CON = \sum_{r=0}^{L-1} \sum_{c=0}^{L-1} \left(r-c\right)^2 P(r,c) \quad (20)$$

3. Results and Discussion

Figure 7 presents the state of granite after being heated to various target temperatures and subsequently cooled in a 15 °C environment. It is observed that with the increase in thermal disturbance temperature, the color of the rock samples shifts from light white-gray to light brown. The quantity of biotite in the samples decreases, but its color becomes particularly prominent. Additionally, it is noticeable that after 400 °C, the surface of the samples is densely covered with many intergranular cracks, and the crystals of feldspar and quartz become increasingly distinct.

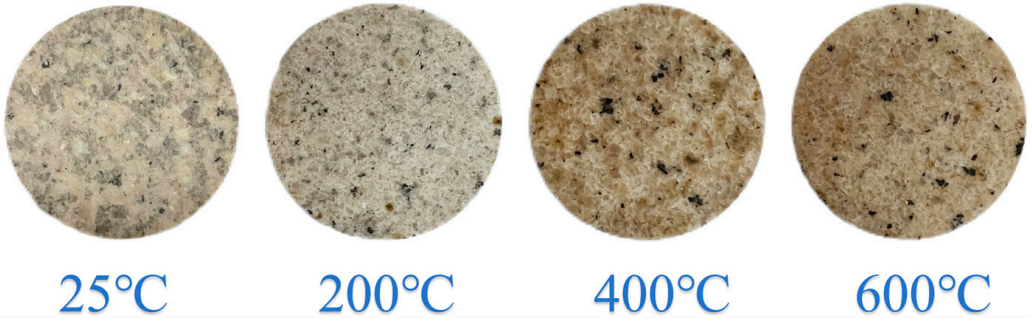
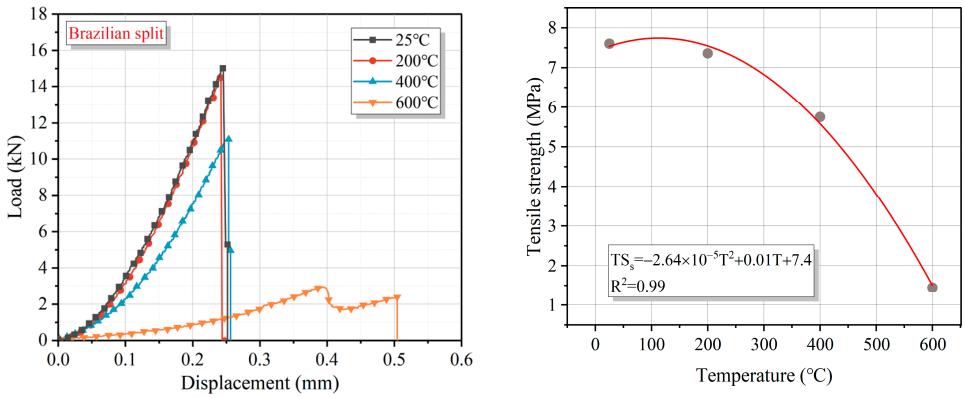


Figure 7. Cross-section of granite after heat treatment.

3.1. Brazilian Test Mechanics and Acoustic Emission Patterns

Figure 8 presents the load–displacement curves and tensile strength distribution patterns of granite undergoing Brazilian test under various non-steady-state thermal disturbance conditions. Generally, the load–displacement curve of Brazilian test specimens can be divided into compaction, elastic, plastic, and unloading phases. In the results of this test, all specimens exhibited a compaction phase, which increased in extent and became more pronounced with rising temperature, especially at thermal disturbance temperatures of 400 °C and 600 °C. Regarding the elastic phase, the higher the thermal disturbance temperature, the shorter and less pronounced the elastic phase becomes. Furthermore, given that granite is a typical representative of quasi-brittle rocks, its compression phase is generally shorter and less noticeable compared to porous rocks such as sandstone, mudstone, and shale [57,58], with the only hysteresis phenomenon in the unloading phase observed at 600 °C.



(**a**) (**b**)

Figure 8. Results of the Brazilian test under different thermal disturbance levels: (**a**) displacement-load curve and (**b**) tensile strength.

Moreover, it is observed that different levels of thermal disturbance temperatures have a distinctly negative trend on the tensile properties of the specimens, with a decline starting at 400 °C and most pronounced at 600 °C. The deterioration in tensile properties is reflected in the reduction in peak load levels and the increase in peak displacement scales. In the Brazilian test, the relationship between the time-dependent load parameters and the tensile stress at the center of the disc specimen is as follows:

$$\sigma_t(t) = \frac{2F(t)}{\pi DL} \tag{21}$$

where $\sigma_t(t)$ is the tensile stress at the center of the disc specimen at loading time t, in MPa; $F(t)$ is the load applied to the specimen at time t, in N; D is the diameter of the specimen, in mm; L is the length of the specimen, which for a disc specimen is the thickness or height, in mm. The Brazilian disc tensile strength can be calculated using the peak load applied to the specimen.

From Figure 8b, it is evident that there is a significant non-linear negative correlation between the Brazilian test tensile strength of the specimens and the level of thermal disturbance. This is corroborated by the fitting equation's R^2 value, which is greater than 0.95. Specifically, a slight reduction in Brazilian test tensile strength is observed at 200 °C, with a decrease of 3.19% relative to the value at 25 °C. As the temperature increases, the tensile strength continues to decrease, reaching a reduction of 24.36% at 400 °C. Notably, the largest decrease occurs at 600 °C, with a significant reduction of 80.95%.

In the deformation and failure process of rock-like materials under external forces, the generation of inherent and secondary cracks, their nucleation, and the macroscopic crack propagation are all accompanied by unidirectional energy conversion, specifically the transformation of mechanical energy into acoustic energy. Utilizing AE technology, it is possible to monitor and capture AE signals in real-time during the loading of specimens. The evolution of damage in rock specimen fracture and instability can be described based on the variation in AE parameters, such as AE ring-down counts and cumulative ring-down counts. Figure 9 illustrates the temporal evolution of deformation, load, and AE events during the Brazilian test process of granite under different levels of thermal disturbance. It is evident that there is a significant correlation between the loading phase, AE events, and the load and displacement during the loading process. With increasing thermal disturbance temperature, the number of AE events increases, as does the cumulative count of AE events. The entire loading process can be divided into: (I) Microcrack Closure Stage, (II) Elastic Deformation Stage, (III) Crack Stable Propagation Stage, and (IV) Post-Peak Stage [59]. As observed in the figure, during the Microcrack Closure Stage, there is a minor release of energy due to the compaction of cracks, but virtually no energy release occurs during

the Elastic Stage, which is evident from the AE event curve. As the load increases, the Elastic Deformation Stage rapidly accumulates energy, and upon entering the Crack Stable Propagation Stage, the AE timing begins to accumulate rapidly. Entering the Post-Peak Stage, the stored elastic energy is released swiftly, leading to the instantaneous failure of the specimen, accompanied by a surge in AE events.

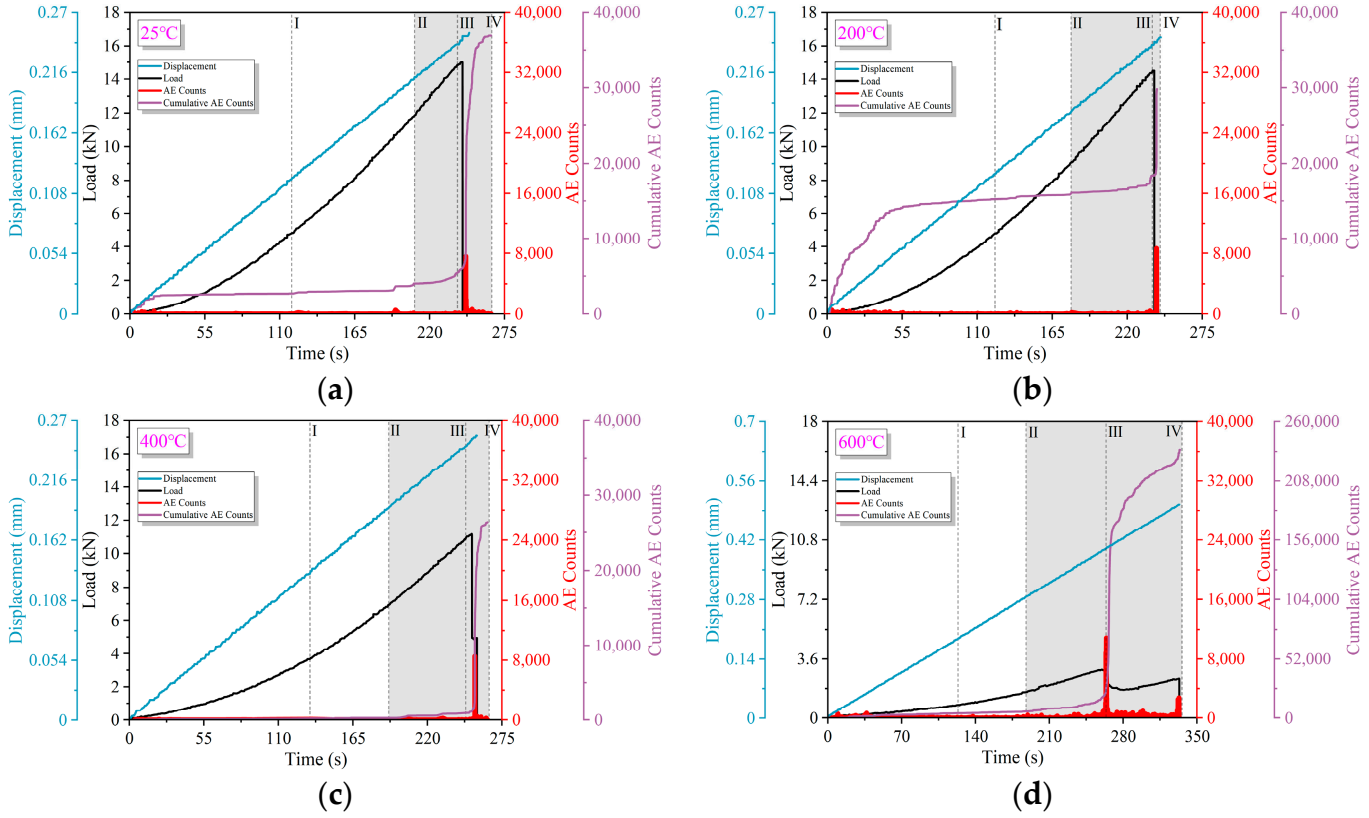


Figure 9. Load and acoustic emission history during the Brazilian test process of granite under different levels of thermal disturbance: (**a**) 25 °C, (**b**) 200 °C, (**c**) 400 °C and (**d**) 600 °C. The boundary lines drawn in these figures are based on an integrated consideration of the load–displacement, load–time and AE characteristics, but this demarcation is qualitative rather than quantitative.

Furthermore, it is observed that as the temperature increases, the number of AE events within the samples consistently rises. For instance, between temperatures of 25 and 400 °C (Figure 9a–c), both the load and the duration of acoustic emissions remained below 275 s. It was only at a temperature of 600 °C that the samples experienced failure at approximately 270 s, with the peak displacement being more than double that at other temperatures. This is primarily due to a series of activities in the granite, such as thermal expansion, dehydration, thermal decomposition, and phase transformation at 600 °C, with the most representative being the phase transition of α-quartz to β-quartz at 573 °C [13,60,61]. These activities disrupt the rock's native framework, increase the spacing between mineral grains, and promote the development of secondary defects, thereby reducing the brittleness and increasing the ductility of the samples. This necessitates a greater dissipation of energy to develop macroscopic crack paths during the loading process. AE events during the compaction phase are somewhat suppressed, and the duration of the elastic phase also degrades. The intensity of AE timing in the post-peak phase shows variation, with higher temperatures leading to a greater number of residual AE events post-peak, thereby prolonging the duration. Research has found that the more ductile the rock material, the more pronounced is the continuous monitorability of AE during the post-peak phase [43].

3.2. Planar Strain Field Evolution Pattern

A CCD camera can record the deformation and crack propagation evolution of granite specimens during the loading process. Figure 10 displays the planar (horizontal, x-direction) strain fields corresponding to 30%, 50%, 70%, 90%, 95%, 99%, and 100% (peak load) of the peak load during the Brazilian test of granite under different thermal disturbance levels. From the figure, it is evident that as the Brazilian test specimens approach the peak load, both the extremity and range of the surface horizontal strain increase. Furthermore, the surface strain and cracks are predominantly tensile, with the compression phase being almost negligible. It is also noted that the 30% and 50% stages of the peak load represent rapid accumulation zones of strain, corresponding to the Microcrack Closure Stage (I) and Elastic Deformation Stage (II) in the load–displacement and acoustic emission processes. Subsequently, cracks begin to develop along the areas of concentrated strain, leading to splitting failure. This stage primarily occurs between 70% and 95% of the peak load, corresponding to the Crack Stable Propagation Stage (III) in the load–displacement and acoustic emission processes.

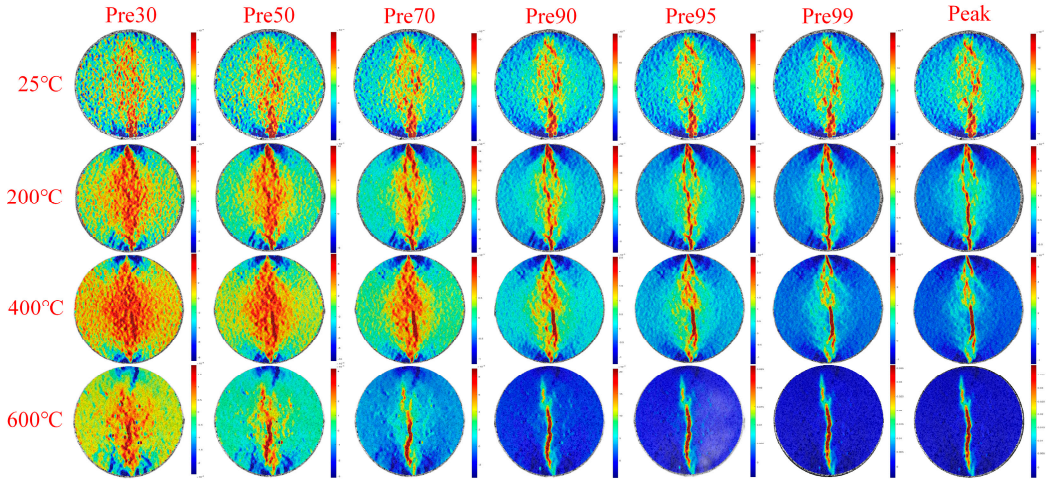


Figure 10. The strain fields in the x-direction corresponding to 30%, 50%, 70%, 90%, 95%, 99%, and the peak load during the Brazilian test of granite under different levels of thermal disturbance.

Typically, the location of maximum tensile strain is described as a transition in the failure mode between shear and tensile failures (Figure 11a [62]), with the central crack line GH observed in the Brazilian Disc Test being related to the tensile failure mode. Figure 11b [63] illustrates the numerical simulation results obtained after importing brick and wedge meshes constructed using ANSYS into FLAC3D, showing the normalized principal stress on the surface plane and the mid-plane of the disk for diameter AB. A uniform load was applied vertically at a rate of 0.2 N/step to each mesh point within the loading strip, sustained for 2000 steps, and then held constant until the model achieved final mechanical equilibrium. The results show that the distribution of tensile stress (σ_{xx}) on the surface plane differs from that on the mid-plane, while the distribution of compressive stress (σ_{zz}) is essentially the same on both planes. This disparity is likely to play a dominant role in the initiation of cracking behavior. However, in previous experimental studies, it has been difficult to determine whether tensile fractures propagate from point G (H) towards the center or from the center towards point G (H). DIC technology perfectly resolves this issue. Monitoring results show that while cracks initiate in the central part, the strain concentration area actually starts developing from the loading end towards the center of the specimen, accompanied by the fusion of microstrains forming the deformation concentration area. Additionally, in terms of thermal disturbance temperature levels, the horizontal strain field in Brazilian test also shows a positive response. Overall, with the rise in thermal disturbance temperature, both the peak strain values and the area of high strain distribution at the same percentage stage of peak load increase, especially after 400 °C.

Secondly, the higher the thermal disturbance temperature level, the lower the percentage stage of peak load at which cracking initiates in the center of the Brazilian test specimens. For instance, at 400 °C, cracks are already formed at 50% of the peak load, whereas similar cracks at 25 °C and 200 °C appear only after 90% of the peak load. This phenomenon is further intensified at 600 °C.

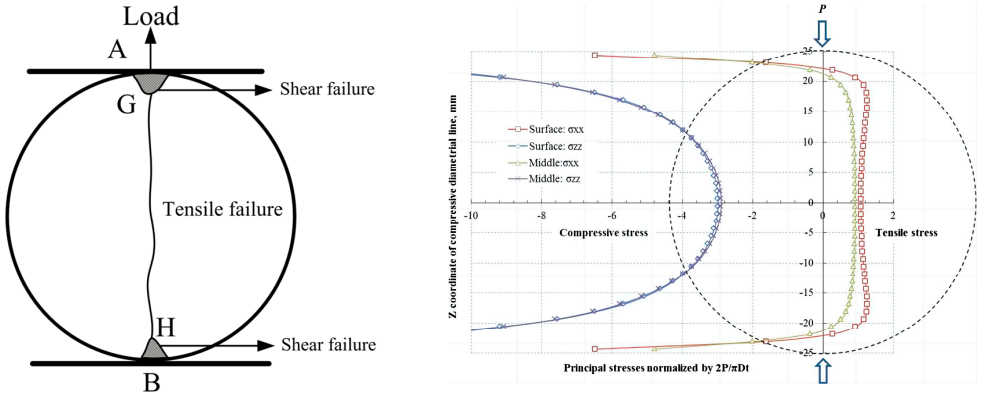


Figure 11. (**a**)The transition between shear and tensile failure modes in solid discs during the Brazilian split test [62], and (**b**) normalized principal stress simulation results along the compression diameter line between the surface and the middle part of the Brazilian disc specimens, with dashed circles indicating the Brazilian disc specimens [63].

To investigate the displacement changes in the specimen in the X direction during the loading process, two horizontal points, A and B, along the X direction and passing through the center of the circle, were marked using DIC, as shown in Figure 12a. By calculating the distance between these two horizontal points, the displacement change in the X direction (lateral displacement) of the specimen during loading can be determined. It is not difficult to observe that as the lateral displacement approaches the peak load, the displacement increases. Specifically, when the load reaches 80% of its peak value, a significant leap in lateral displacement can be observed at almost all thermal disturbance temperature levels. This leap is most pronounced after reaching 95% of the peak load. Figure 12b presents the displacement change information under different thermal disturbance levels. It is evident that the displacement exhibits a positive response to thermal disturbance temperatures, with the relationship displaying a non-linear positive correlation. At a temperature of 200 °C, the displacement expansion growth rate increased by 55.93% compared to 25 °C. At 400 °C, this growth rate continued to rise relative to 200 °C, reaching an increase of 94.77% compared to 25 °C. When the thermal disturbance temperature reached 600 °C, the displacement expansion growth rate experienced a dramatic increase, with a rise of 435.47% compared to 25 °C.

3.3. Digital 3D Fracture Surface Fractals and Roughness Response

The three-dimensional digital fracture surfaces of granite after Brazilian test at different thermal disturbance temperature levels are provided in Figure 13. It can be observed that the morphological characteristics of the three-dimensional digital fracture surfaces exhibit visually distinct differences influenced by temperature, which manifest as variations in elevation on the horizontal plane. Typically, it can be observed that as the temperature increases, the area with elevations greater than 0.9 experiences compression, and the undulating morphology undergoes changes.

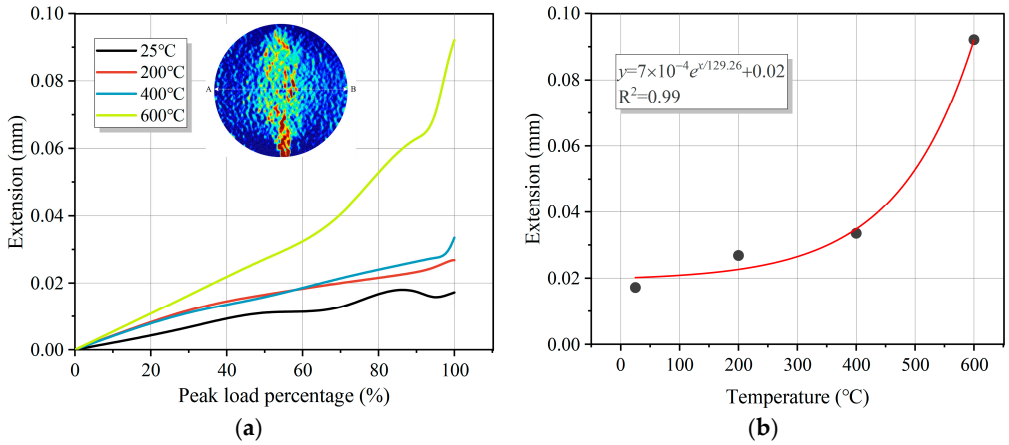


Figure 12. Surface strain information of Brazilian test specimens under different thermal disturbance levels during the loading process: (**a**) the evolution of lateral displacement, namely the distance between points A and B, at different peak load stages, and (**b**) the fitted relationship between various thermal disturbance levels and the maximum lateral displacement.

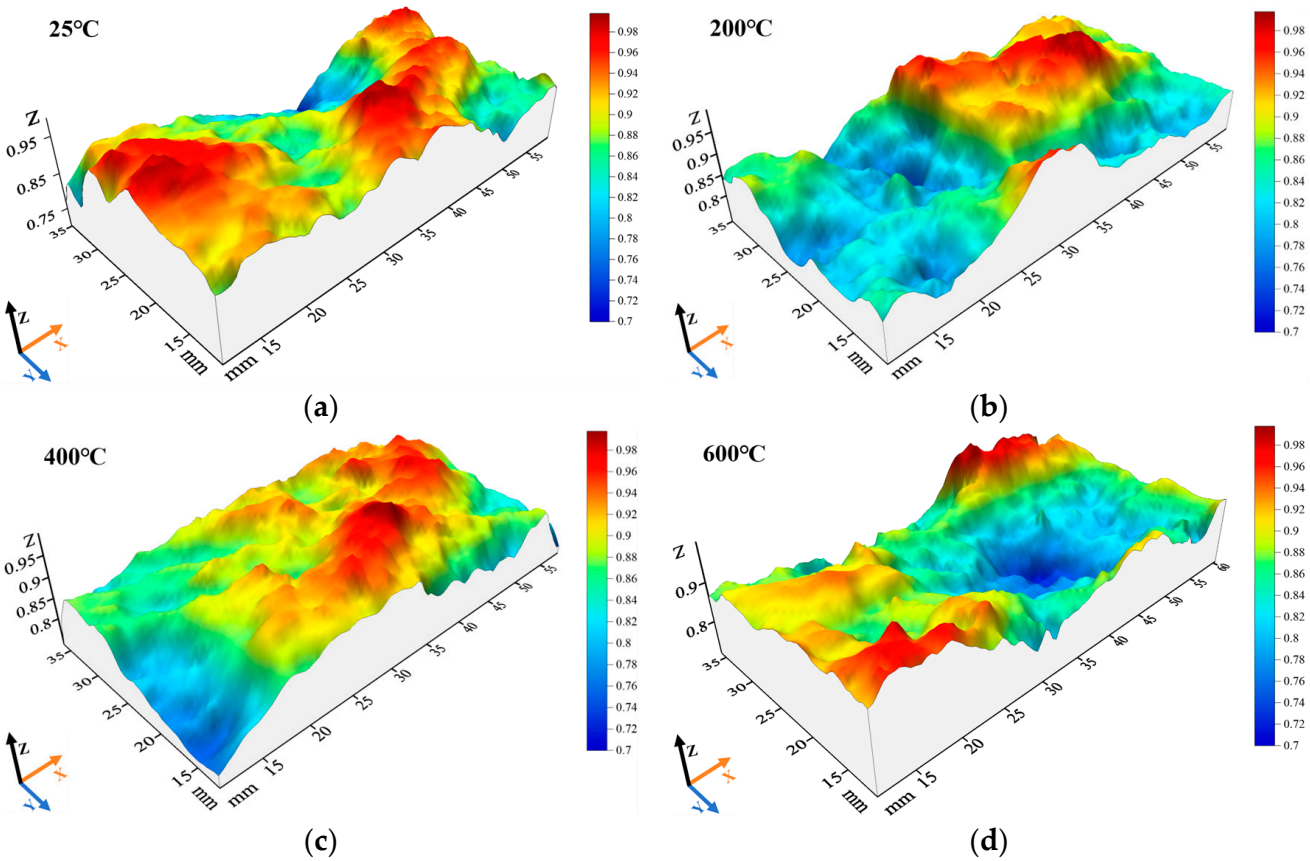


Figure 13. The three-dimensional digital fracture surfaces of Brazilian splitting at various thermal disturbance levels, with the elevation values normalized: (**a**) 25 °C, (**b**) 200 °C, (**c**) 400 °C and (**d**) 600 °C.

To further characterize and analyze this variation, the digital fracture surfaces of granite after Brazilian test, treated at different thermal disturbance temperature levels, were covered and counted using the box-counting method as described above, yielding lnN and $ln\delta$ fitting results, as shown in Figure 14. It can be observed that the R^2 for all fracture surfaces are 0.98, indicating the reliability of the fitting results. The distribution patterns of the fitting curves and data points exhibit significant similarities at a macroscopic level.

Additionally, the influence of thermal disturbance temperature on the fractal dimension of the specimen's fracture surfaces is relatively small, with the main magnitude concentrated in the range of 0.001–0.01. To some extent, this similarity in accuracy with the fractal dimensions of mode-I fractures in thermally treated granite and dynamic fissured sandstone subjected to low-cycle impact as observed by Yin et al. [35] and Chen et al. [64].

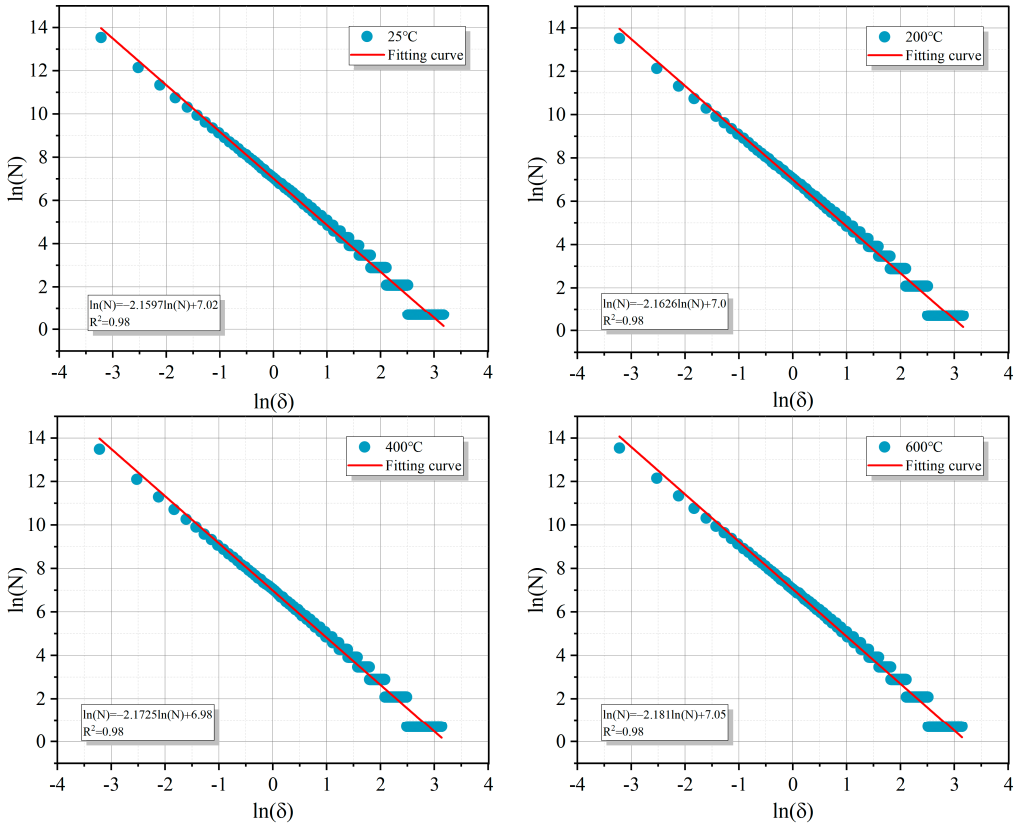


Figure 14. The fitting relationships between $ln(N)$ and $ln(\delta)$ for the three-dimensional digitized Brazilian fracture surfaces using the box-counting method.

Therefore, the fractal dimension was analyzed with an accuracy of 0.001, and the corresponding fractal dimensions obtained from calculations were plotted in Figure 15. It is evident that within this precision range, the influence of thermal disturbance temperature on the Brazilian splitting surface of granite becomes more pronounced. Overall, as the heat treatment temperature increases, the fractal dimension also relatively increases. Specifically, the impact of thermal disturbance temperature on the sample's fractal dimension exhibits consistency, but the degree of influence varies. For example, the fractal dimension of the sample surface at 200 °C increased by 0.13% relative to 25 °C, while at 400 °C, the fractal dimension of the sample surface increased significantly compared to 200 °C, with a relative increase of 0.59% relative to 25 °C. It is worth noting that when the thermal disturbance temperature reaches 600 °C, the fractal dimension of the sample surface relative to 25 °C only reaches a 0.99% increase, but this is already the peak. Furthermore, there is a significant linear positive correlation between the fractal dimension and the thermal disturbance temperature, as evidenced by an R^2 value of 0.96.

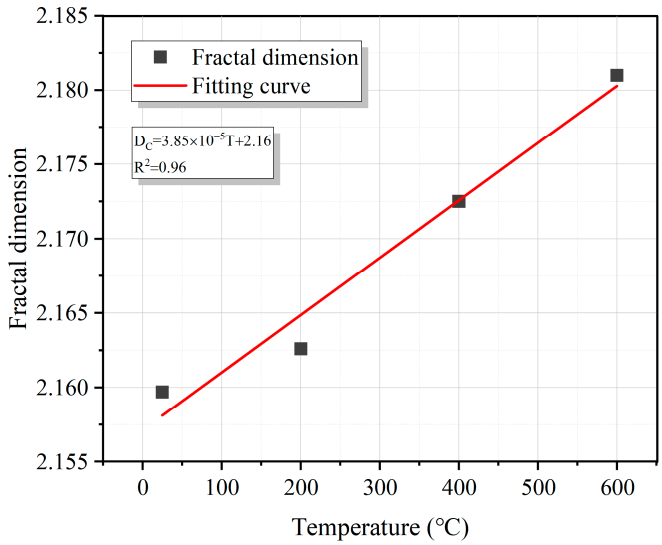


Figure 15. The fitting relationships between thermal disturbance levels and three-dimensional fractal dimensions of Brazilian splitting surfaces.

Figure 16 illustrates the impact of thermal disturbance temperature on roughness parameters. Unlike the linear relationship observed with fractal dimensions, there exists a non-linear correlation, albeit without an R^2 similar to the reliability demonstrated by R^2 for fractal dimensions; the maximum R^2 observed is 0.82, as shown in R_z. Specifically, R_a, R_z, and R_q exhibit similar response behaviors to thermal disturbance temperature, all decreasing between 25 and 200 °C and increasing between 400 and 600 °C. This indicates that as the thermal disturbance temperature rises to 200 °C, the Brazilian splitting surface of granite becomes smoother, with reduced extreme height variations, resulting in a more uniform surface, and a noticeable decrease in roughness. When the thermal disturbance temperature reaches 400 and 600 °C, the unevenness of the Brazilian splitting surface of granite starts to increase, with a larger difference between the highest and lowest points, an overall increase in surface variation, a more uneven distribution of microcracks, and an increase in roughness. It is noteworthy that the rate of decline in roughness between 25 and 200 °C is significantly higher than the rate of increase. Similar response characteristics have also been reported by Nasseri et al. [64].

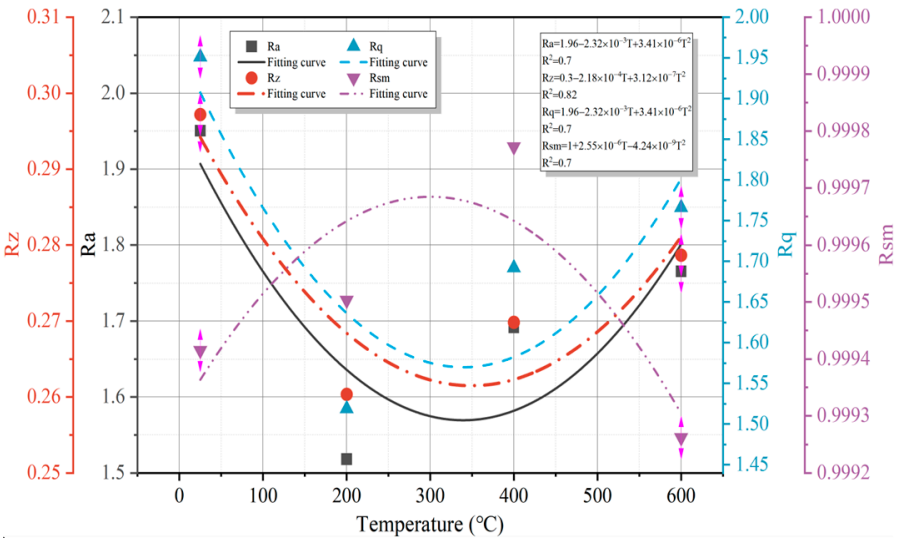
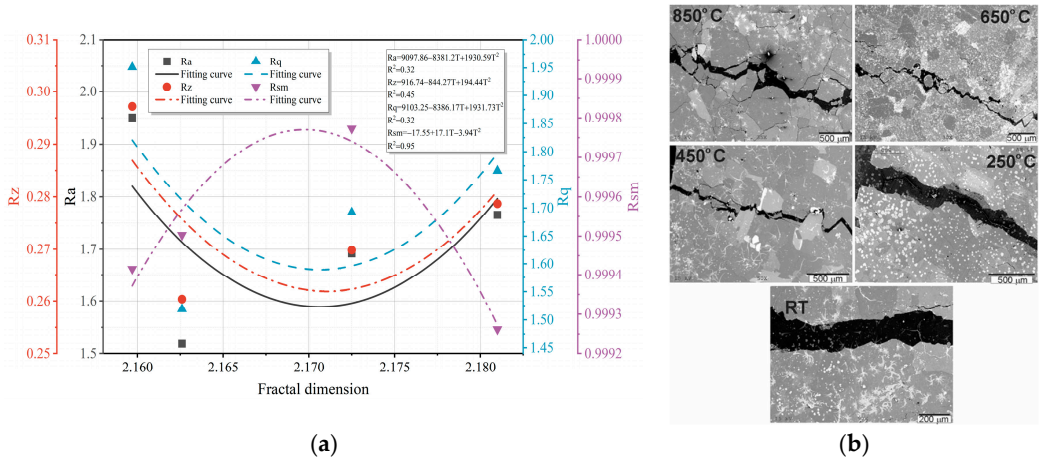


Figure 16. Roughness parameters of three-dimensional digitized Brazilian splitting surfaces under different thermal disturbance levels.

On the other hand, the behavior of R_{sm} with respect to thermal disturbance temperature is essentially opposite to that of R_a, R_z, and R_q. It continues to increase between 25 and 400 °C but experiences a sudden drop at 600 °C, even falling below the initial value at 25°C. This suggests that the slope between adjacent point clouds on the Brazilian splitting surface of granite increases between 25 and 400 °C, indicating more irregular variations on the fracture surface, which could lead to an increase in roughness. At 600 °C, it indicates that the slope of the fracture surface becomes gentler, possibly resulting in a reduction in roughness.

Figure 17a presents the response patterns of the three-dimensional fractal dimensions of Brazilian splitting surfaces in granite concerning roughness parameters R_a, R_z, R_q, and R_{sm}. In general, there appears to be some form of non-linear correlations between the fractal dimension and these roughness parameters. However, the fitting results indicate that except for an R^2 of 0.95 with respect to R_{sm}, the reliability of the fitting with R_a, R_z, and R_q ranges from 0.32 to 0.45, which can essentially be disregarded. Here, only the validity of the linear relationship between R_{sm} and the fractal dimension response is considered.



(**a**) (**b**)

Figure 17. (**a**) The fitting relationship between roughness parameters and fractal dimensions of three-dimensional digital Brazilian fracture surfaces. (**b**) SEM images of thin sections from thermally treated Westerly granite [65].

It can be observed that the response behavior of R_{sm} on temperature for the Brazilian splitting surface of granite exhibits a high degree of consistency with the response behavior to the fractal dimension. It shows an upward trend between 2.1597 and 2.1725 but experiences a sudden drop at 2.181, completely negating the increase within the 2.1597–2.1725 range, such that the value at 600 °C even falls below the initial value. With the assumption of the exclusion of outliers in R_{sm} at 600 °C and 2.181, it can be argued that within the tested thermal disturbance range, R_{sm} in Brazilian splitting surfaces of granite holds potential value in predicting the fractal dimension.

Generally, the partial cause of the temperature-responsive characteristics of roughness and fractal features stems from the differential thermal expansion of quartz, feldspar, and mica minerals. As temperature escalates to 200 °C, minerals within the rock expand at disparate rates, leading to an increase in internal stresses and intergranular compression, rendering the mineral assembly more compact. With further elevation of temperature to 400 °C and 600 °C, this uneven expansion exacerbates, and the volume of quartz phase transitions further enlarges, culminating in the genesis of microcracks and particle detachment on the rock's surface. Moreover, pre-existing microcracks within the rock might widen and interconnect under the influence of thermal stresses. On another note, SEM images depicting the development of tensile cracks in granite after undergoing thermal treatments at varying temperatures, as shown in Figure 17b, significantly illustrate that the crack propagation path is considerably constrained by temperature. Below 250 °C, cracks are predominantly observed to traverse directly through the grains (transgranular

cracks), whereas above 450 °C, cracks principally develop along the intergranular gaps induced by thermal stresses (intergranular cracks). This occurs because, according to the principle of minimum energy or the energy release rate criterion [66–68], cracks propagate in the direction where the energy release rate is maximized, usually implying the path of least resistance. The path along grain boundaries is inherently more meandering than the transgranular path, thereby significantly increasing the fractal dimension. These factors collectively govern the macroscopic fracture surface roughness and fractal dimension of granite Brazilian test specimens, alongside other morphological characteristics including texture and elevation information.

3.4. Statistical Characteristics of Digital Image of Fracture Surfaces Based on GLCM

The two-dimensional digitalized granite Brazilian fracture surfaces before and after grayscale transformation are depicted in Figure 18. The incident light angle was fixed at 60° to ensure the comparability of image grayscale. The grayscale values corresponding to the two-dimensional fracture surfaces ranged from 0 to 255. On the basis of grayscale attributes, grayscale co-occurrence matrices were constructed for each fracture surface image, and second-order statistical measures representing texture characteristics were computed. It is worth noting that grayscale values also exhibit varying responses to thermal disturbance temperatures.

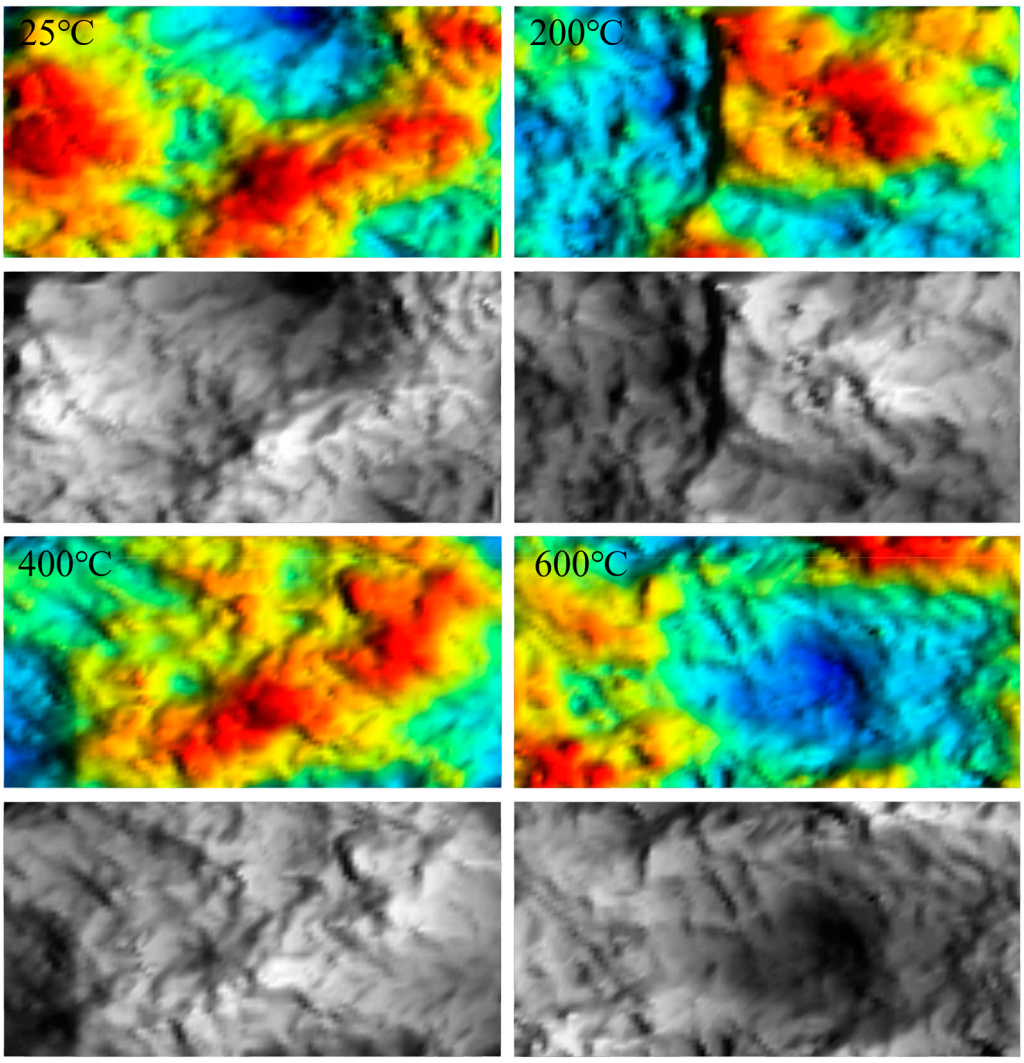


Figure 18. The two-dimensional digital Brazilian fracture surfaces of granite before and after grayscale transformation.

Figure 19 describes four second-order statistical measures (*ASM*, *COR*, *ENT*, and *CON*), as well as their averages, derived from the 0°, 45°, 90°, and 135° orientations within the GLCM of the digitized Brazilian fracture surfaces. Among these, *ASM* reflects the uniformity of image grayscale distribution and texture thickness, with rougher textures corresponding to higher *ASM* values. It is evident that thermal disturbance temperature positively impacts *ASM* in various directions within the GLCM, as indicated by a consistent standard deviation, demonstrating a considerable uniformity in response trends. The relationship between *ASM* and thermal disturbance temperature is conspicuously non-linear and positive. At 200 °C, the average *ASM* exhibits a relatively moderate increase of 4.75% compared to 25 °C. This increment rises to 16.28% at 400 °C and peaks at 600 °C with a 39.65% increase. Similarly, the behavior of *COR* parallels *ASM*, with a stable standard deviation ranging from 1.93652×10^{-4} to 8.61324×10^{-4}, suggesting that the influence of different orientation angles in the fracture surface GLCM is negligible. In other words, the textural similarity of the fracture surface is, to some extent, induced by rising thermal disturbance temperatures. *ENT*, reflecting the amount of information contained in the image, increases with more complex textures. The behavior of *ENT* in the GLCM is more distinctly affected by directional angles compared to *ASM* and *COR*. However, its response to thermal disturbance temperatures is largely inverse to that of *ASM* and *COR*. Overall, the effect of thermal disturbance temperature on *ENT* is negative, with fitting results showing a significant non-linear negative correlation. The average *ENT* at 200 °C shows a relatively aggressive deterioration of 3.01% compared to 25 °C. This reduction expands to 4.84% at 400 °C and peaks at 9.62% at 600 °C, indicating that increased thermal disturbance temperatures reduce the complexity of the texture distribution of the Brazilian split granite fracture surface. The behavior of *CON* is similar to *ENT*, and the fluctuations caused by the directional orientations of the GLCM are more aggressive. However, rising thermal disturbance temperatures have a role in reducing the standard deviation.

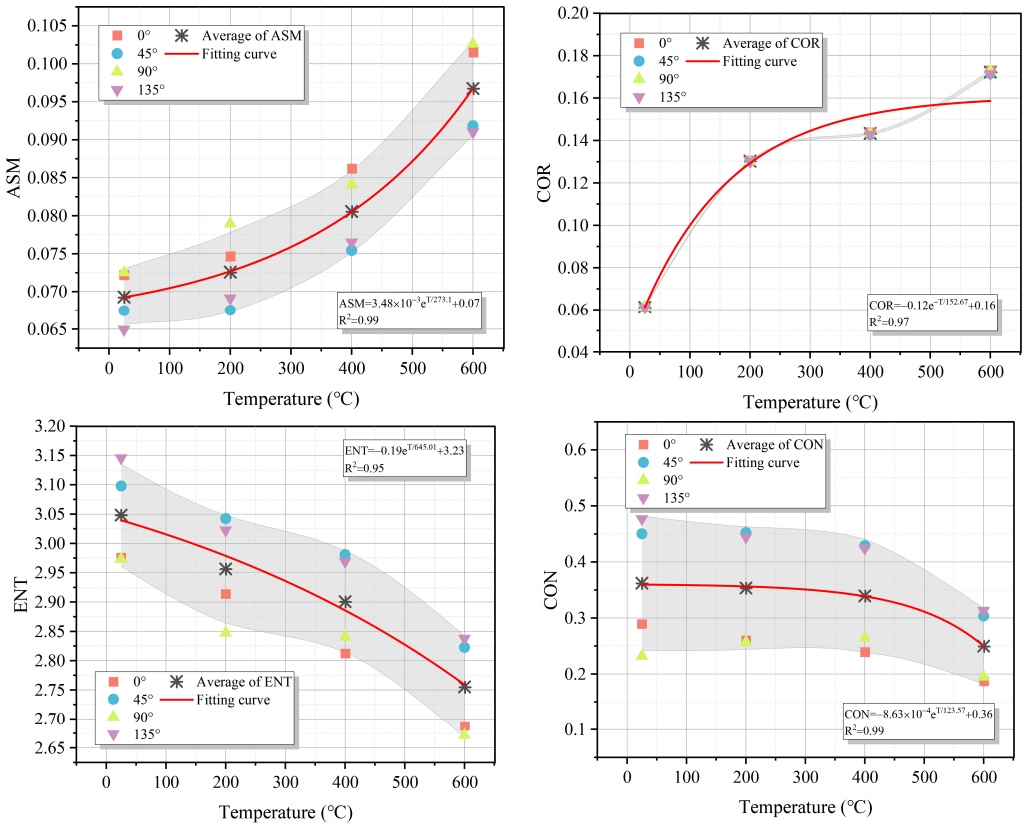


Figure 19. Second-order statistical metrics of 3D digitized Brazilian fracture surfaces under different thermal disturbance levels, the shaded regions indicate the standard deviations.

Figure 20 depicts the normalized elevation characteristics of the digitized Brazilian fracture surface of granite after treatment at different thermal disturbance temperature levels. It is observed that at a thermal disturbance temperature of 25 °C, the variation pattern of the fracture surface elevation characteristics of the sample is relatively stable. The overall normalized elevation values are concentrated above 0.9, with a uniform distribution and minimal undulations, forming an elevation value distribution pattern resembling valley terrain. At 200 °C, there is a change in the variation pattern of the fracture surface elevation characteristics of the sample. The proportion of overall normalized elevation values concentrated above 0.9 begins to decrease, and the distribution starts to become uneven, with increased undulations, deteriorating the trend of forming a valley-like elevation value distribution pattern. When the thermal disturbance temperature reaches 400 °C, the portion of the sample's fracture surface with overall normalized elevation values above 0.9 continues to decrease, and the uniformity of the distribution further diminishes, forming an elevation value distribution pattern akin to mountainous terrain. At a thermal disturbance temperature of 600 °C, a significant change is noted in the elevation characteristics of the fracture surface. The area of the fracture surface with elevation values below 0.9 increases sharply, while the area with elevation values above 0.9 drastically reduces, now constituting less than 20% of the area, forming an elevation value distribution pattern resembling basin-like terrain.

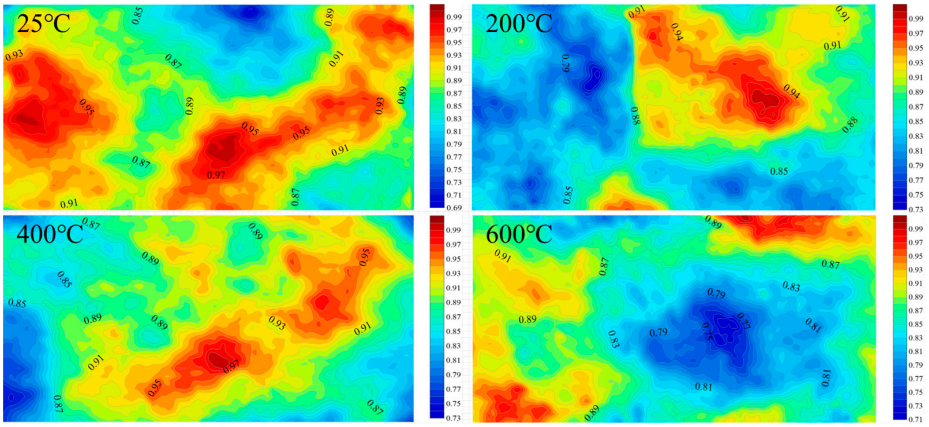


Figure 20. Normalized 2D elevation of digital fracture surface of Brazilian splitting under different thermal disturbance levels.

A statistical analysis was conducted on the elevation distribution characteristics of the digitized fracture surface. The analysis parameters included range, interquartile range (IOR, S_I), average (S_A), coefficient of variation (S_{CV}), variance (S_V), standard deviation (S_{SD}), Kurtosis (S_K), and skewness (S_S). The formulas for calculating each of these parameters are as follows:

$$\begin{cases} \text{Range} : S_R = \max(z) - \min(z) \\ \text{IQR} : S_I = Q_3(z) - Q_1(z) \\ \text{Average} : S_A = \frac{1}{n}\sum_{i=1}^{n} z_i \\ \text{Coefficient of variation} : S_{CV} = \frac{\sqrt{\frac{1}{n}\sum_{i=1}^{n}\left(z_i - \frac{1}{n}\sum_{j=1}^{n} z_j\right)^2}}{\frac{1}{n}\sum_{i=1}^{n} z_i} \\ \text{Variance} : S_V = \frac{1}{n}\sum_{i=1}^{n}\left(z_i - \frac{1}{n}\sum_{j=1}^{n} z_j\right)^2 \\ \text{Standard Deviation} : S_{SD} = \sqrt{\frac{1}{n}\sum_{i=1}^{n}\left(z_i - \frac{1}{n}\sum_{j=1}^{n} z_j\right)^2} \\ \text{Kurtosis} : S_K = \frac{\frac{1}{n}\sum_{i=1}^{n}(z_i - \bar{z})^4}{\left(\frac{1}{n}\sum_{i=1}^{n}(z_i - \bar{z})^2\right)^2} \\ \text{Skewness} : S_S = \frac{\frac{1}{n}\sum_{i=1}^{n}(z_i - \bar{z})^3}{\left(\frac{1}{n}\sum_{i=1}^{n}(z_i - \bar{z})^2\right)^{\frac{3}{2}}} \end{cases} \quad (22)$$

Here, $Q_3(z)$ and $Q_1(z)$ would be the values at the 75th and 25th percentiles of the dataset z, respectively.

The differential impact of thermal disturbance on the Brazilian fracture surface of granite is primarily manifested through its influence on the distribution of elevation values. As depicted in Figure 21, there exist significant non-linear correlations between thermal disturbance temperatures and these statistical parameters, with R^2 values ranging between 0.91 and 0.99. The fitting results for each parameter with respect to thermal disturbance temperatures are also presented in the figure. Concerning range and IQR, the impact of thermal disturbance temperatures shows high similarity, with low-level fluctuations between 25 °C and 400 °C, but a sudden, marked increase at 600 °C. A similar response pattern is observed in the coefficient of variation, variance, and standard deviation, suggesting the likely existence of a critical temperature point between 400 °C and 600 °C, at which a dramatic change in elevation characteristics occurs. Regarding the Average, this value is in a declining state between 25 °C and 400 °C, with an upward shift occurring at 600 °C. This transition point for Skewness begins at 200 °C. Kurtosis is the only parameter exhibiting a monotonic non-linear negative correlation with thermal disturbance temperature, indicating that thermal disturbance significantly degrades both the tail and the high peak of the elevation data of the granite Brazilian fracture surface.

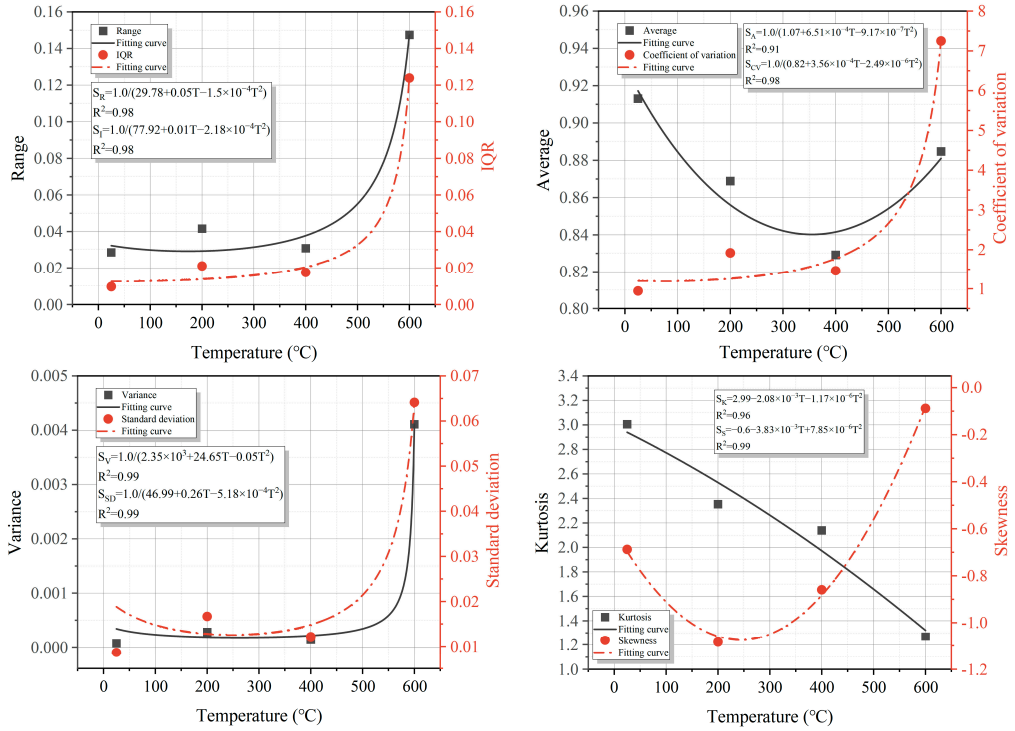


Figure 21. Statistical analysis of three-dimensional digital fracture elevation in Brazilian split tests at various thermal disturbance levels.

4. Conclusions

This paper systematically documents the research findings on the mechanical response and digital fracture characteristics of granite following non-steady-state thermal disturbance in laboratory Brazilian tests. This study examines the specimen's mechanical parameters, acoustic emission behavior, evolution of the surface strain field, and characteristics of the digitized fracture morphology. The main conclusions are summarized as follows:

(1) There is a significant degradation in the tensile strength of the specimens due to thermal disturbance temperatures, with reductions reaching 24.36% at 400 °C and 80.95% at 600 °C.

(2) The number of acoustic emission events displayed a sudden increase at 600 °C, where the post-peak phase acoustic emissions' monitorability was also most significant.
(3) With increasing temperature, the load level at which cracking initiates in the center of the Brazilian samples is lower, and the areas of high strain are more concentrated. Consequently, there is a greater rate of horizontal displacement expansion in the center of the specimens, especially at 600 °C.
(4) There is a linear positive correlation between thermal disturbance temperature and the fractal dimension of the fracture surface, a relatively moderate non-linear relationship with R_z, and R_{sm} shows potential value in predicting the fractal dimension.
(5) The four second-order statistical measures of the digitized fracture surface's GLCM exhibit a high dependency on thermal disturbance temperature.
(6) The statistical parameters of the elevation values for the digitized fracture surface exhibit a significant non-linear relationship with temperature, with the critical threshold temperature for abrupt changes in elevation characteristics anticipated to be between 400 and 600 °C.

Author Contributions: Conceptualization, Y.C.; methodology, Y.C.; software, Y.C.; validation, Y.C. and T.Y., formal analysis, Y.C.; investigation, Y.C.; resources, Y.C.; data curation, Y.C.; writing—original draft preparation, Y.C.; writing—review and editing, T.Y. and Y.C.; visualization, Y.C.; supervision, Y.C. and T.Y.; project administration, T.Y.; funding acquisition, T.Y. and Y.C.; All authors have read and agreed to the published version of the manuscript.

Funding: This work was financially supported by the National Natural Science Foundation of China (No. 41972283); the Fundamental Research Funds for the Central Universities of Central South University (No. 2021zzts0287); the China Scholarship Council (No. 202206370109). We also thank the anonymous reviewers for their valuable comments and suggestions to improve this manuscript.

Data Availability Statement: The data presented in this study are available on request from the corresponding author.

Conflicts of Interest: We declare that we have no financial and personal relationships with other people or organizations that can inappropriately influence our work, there is no professional or other personal interest of any nature or kind in any product, service and/or company that could be construed as influencing the position presented in, or the review of, the manuscript entitled.

References

1. Si, X.; Luo, Y.; Luo, S. Influence of lithology and bedding orientation on failure behavior of "D" shaped tunnel. *Theor. Appl. Fract. Mech.* **2024**, *129*, 104219. [CrossRef]
2. Sharmin, T.; Khan, N.R.; Akram, M.S.; Ehsan, M.M. A State-of-the-Art Review on Geothermal Energy Extraction, Utilization, and Improvement Strategies: Conventional, Hybridized, and Enhanced Geothermal Systems. *Int. J. Thermofluids* **2023**, *18*, 100323. [CrossRef]
3. Zayed, M.E.; Shboul, B.; Yin, H.; Zhao, J.; Zayed, A.A.A. Recent advances in geothermal energy reservoirs modeling: Challenges and potential of thermo-fluid integrated models for reservoir heat extraction and geothermal energy piles design. *J. Energy Storage* **2023**, *62*, 106835. [CrossRef]
4. Voskov, D. High-enthalpy geothermal simulation with continuous localization in physics. *Mathematics* **2022**, *10*, 4328.
5. Krauskopf, K.B. Geology of high-level nuclear waste disposal. *Annu. Rev. Earth Planet. Sci.* **1988**, *16*, 173–200. [CrossRef]
6. Ojovan, M.; Steinmetz, H.J. Approaches to Disposal of Nuclear Waste. *Energies* **2022**, *15*, 7804. [CrossRef]
7. Knobloch, K.; Ulrich, T.; Bahl, C.; Engelbrecht, K. Degradation of a rock bed thermal energy storage system. *Appl. Therm. Eng.* **2022**, *214*, 118823. [CrossRef]
8. Jemmal, Y.; Zari, N.; Asbik, M.; Maaroufi, M. Experimental characterization and thermal performance comparison of six Moroccan rocks used as filler materials in a packed bed storage system. *J. Energy Storage* **2020**, *30*, 101513. [CrossRef]
9. Zhang, W.; Sun, Q.; Zhang, Y.; Xue, L.; Kong, F. Porosity and wave velocity evolution of granite after high-temperature treatment: A review. *Environ. Earth Sci.* **2018**, *77*, 350. [CrossRef]
10. Heuze, F.E. High-temperature mechanical physical and thermal properties of granitic rocks; a review. *Int. J. Rock Mech. Min. Sci.* **1983**, *20*, 3–10. [CrossRef]
11. Yong, C.; Wang, C.Y. Thermally induced acoustic emission in Westerly granite. *Geophys. Res. Lett.* **1980**, *7*, 1089–1092. [CrossRef]
12. Wu, J.W.; Zhao, Y.S.; Mo, Z.J.; Feng, Z.J.; Dong, F.K.; Li, Y. Experimental study of acoustic emission of granite due to thermal cracking under high temperature and isostatic stress. *J. China Coal Soc.* **2012**, *37*, 1111–1117.
13. Yin, T.; Chen, Y.; Li, X.; Li, Q. Effect of high temperature and strain rate on the elastic modulus of rocks: A review. *Int. J. Earth Sci. Geol. Rundsch.* **2021**, *110*, 2639–2660. [CrossRef]

14. Lakirouhani, A.; Asemi, F.; Zohdi, A.; Medzvieckas, J.; Kliukas, R. Physical parameters, tensile and compressive strength of dolomite rock samples: Influence of grain size. *J. Civ. Eng. Manag.* **2020**, *26*, 789–799. [CrossRef]
15. Zhi, L.P.; Xu, J.Y.; Liu, Z.Q.; Liu, S.; Chen, T.F. Research on ultrasonic characteristics and Brazilian splitting-tensile test of granite under post-high temperature. *Rock Soil Mech.* **2012**, *33*, 61–66.
16. Zhao, Z.; Liu, Z.; Pu, H.; Li, X. Effect of thermal treatment on Brazilian tensile strength of granites with different grain size distributions. *Rock Mech. Rock Eng.* **2018**, *51*, 1293–1303. [CrossRef]
17. Liang, M.; Zhang, S.H.; Shu, B. Effect of different cooling ways on Brazilian tension characteristics of heat-treated granite. *J. Water Resour. Water Eng.* **2018**, *29*, 186–193.
18. Jin, P.H.; Hu, Y.Q.; Shao, J.X.; Zhao, G.K.; Zhu, X.Z.; Li, C. Experimental study on physico-mechanical and transport properties of granite subjected to rapid cooling. *Chin. J. Rock Mech. Eng.* **2018**, *37*, 2556–2564. [CrossRef]
19. Yong, Y. Experimental study on Brazilian split test and acoustic emission characteristics of high temperature granite under different cooling methods. *Geol. Sci. Technol. Bull.* **2022**, *41*, 200–207.
20. Ge, Z.; Sun, Q.; Yang, T.; Luo, T.; Jia, H.; Yang, D. Effect of high temperature on mode-I fracture toughness of granite subjected to liquid nitrogen cooling. *Eng. Fract. Mech.* **2021**, *252*, 107834. [CrossRef]
21. Li, Q.; Yin, T.; Li, X.; Shu, R. Experimental and Numerical Investigation on Thermal Damage of Granite Subjected to Heating and Cooling. *Mathematics* **2021**, *9*, 3027. [CrossRef]
22. Ahn, D.; Stevens, L.; Page, Z. Rapid high-resolution visible light 3D printing. *ACS Central Sci.* **2020**, *6*, 1555–1563. [CrossRef] [PubMed]
23. Lipson, H. *Fabricated: The New World of 3D Printing*; John Wiley & Sons: Hoboken, NJ, USA, 2013.
24. Lee, T.; Ramlan, R. An overview on 3D printing technology: Technological, materials, and applications. *Procedia Manuf.* **2019**, *35*, 1286–1296.
25. Kukko, A.; Kaartinen, H.; Hyyppä, J.; Chen, Y. Multiplatform mobile laser scanning: Usability and performance. *Sensors* **2012**, *12*, 11712–11733. [CrossRef]
26. Di Stefano, F.; Chiappini, S.; Gorreja, A. Mobile 3D scan LiDAR: A literature review. *Geomat. Nat. Hazards Risk* **2021**, *12*, 2387–2429. [CrossRef]
27. Mo, P.; Li, Y. Estimating the three-dimensional joint roughness coefficient value of rock fractures. *Bull. Eng. Geol. Environ.* **2019**, *78*, 857–866. [CrossRef]
28. Li, B.; Li, X.; Xiao, W.; Zang, J.; Wang, H. Quantitative study on joint roughness coefficient (JRC) of rock mass. *IOP Conf. Ser. Earth Environ. Sci.* **2019**, *237*, 32013. [CrossRef]
29. Wang, C.; Yong, R. Advances in joint roughness coefficient (JRC) and its engineering applications. *J. Rock Mech. Geotech. Eng.* **2023**, *15*, 3352–3379.
30. Baecher, G. Statistical analysis of rock mass fracturing. *J. Int. Assoc. Math. Geol.* **1983**, *15*, 329–348. [CrossRef]
31. Rong, G. Experimental study of flow characteristics in non-mated rock fractures considering 3D definition of fracture surfaces. *Eng. Geol.* **2017**, *220*, 152–163. [CrossRef]
32. Zhou, H.W.; Xie, H. Direct estimation of the fractal dimensions of a fracture surface of rock. *Surf. Rev. Lett.* **2003**, *10*, 751–762. [CrossRef]
33. Clarke, K. Computation of the fractal dimension of topographic surfaces using the triangular prism surface area method. *Comput. Geosci.* **1986**, *12*, 713–722. [CrossRef]
34. Xie, H.; Wang, J. Direct fractal measurement of fracture surfaces. *Int. J. Solids Struct.* **1999**, *36*, 3073–3084. [CrossRef]
35. Yin, T.; Li, Q.; Li, X. Experimental investigation on mode I fracture characteristics of granite after cyclic heating and cooling treatments. *Eng. Fract. Mech.* **2019**, *222*, 106740. [CrossRef]
36. Chen, Y.; Yin, T.; Li, Q.; Zhuang, D.; Wu, Y.; Jin, F.; Yang, Z. Experimental investigation on the fracture surface features of heat-treated red sandstone containing fissure under constant amplitude low cycle impact using 3D digital reconstruction. *Eng. Fract. Mech.* **2023**, *277*, 109002. [CrossRef]
37. Ulusay, R. *The ISRM Suggested Methods for Rock Characterization, Testing and Monitoring: 2007–2014*; Springer: Berlin/Heidelberg, Germany, 2014.
38. Sutton, M.; Orteu, J.; Schreier, H. *Image Correlation for Shape, Motion and Deformation Measurements: Basic Concepts, Theory and Applications*; Springer Science & Business Media: Berlin/Heidelberg, Germany, 2009.
39. Li, S.; Lin, H.; Hu, S.; Cao, R.; Luo, X. Mechanical behavior of anchored rock with an infilled joint under uniaxial loading revealed by AE and DIC monitoring. *Theor. Appl. Fract. Mech.* **2023**, *123*, 103709. [CrossRef]
40. Lu, H.; Chen, Q.; Ma, X. Investigation into Dynamic Behaviors of High-Temperature Sandstone under Cyclic Impact Loading Using DIC Technology. *Appl. Sci.* **2022**, *12*, 9247. [CrossRef]
41. Schreier, H.; Orteu, J.; Sutton, M. *Image Correlation for Shape, Motion and Deformation Measurements: Basic Concepts, Theory and Applications*; Springer: Boston, MA, USA, 2009.
42. Reu, P. Introduction to Digital Image Correlation: Best Practices and Applications. *Exp. Tech.* **2012**, *36*, 3–4. [CrossRef]
43. Lockner, D. The role of acoustic emission in the study of rock fracture. *Int. J. Rock Mech. Min. Sci. Geomech. Abstr.* **1993**, *30*, 883–899. [CrossRef]
44. DIC Algorithms. Available online: http://www.ncorr.com/index.php/dic-algorithms (accessed on 29 January 2024).
45. Xie, H.P.; Pariseau, W.G. Fractal estimation of rock joints roughness coefficients (JRC). *Sci. China* **1994**, *24*, 524–530.

46. Ai, T.; Zhang, R.; Zhou, H.W.; Pei, J.L. Box-counting methods to directly estimate the fractal dimension of a rock surface. *Appl. Surf. Sci.* **2014**, *314*, 610–621. [CrossRef]
47. Renaud, S.; Rivard, P. Roughness effects on the shear strength of concrete and rock joints in dams based on experimental data. *Rock Mech. Rock Eng.* **2019**, *52*, 3867–3888. [CrossRef]
48. Gao, G.; Meguid, M. On the role of joint roughness on the micromechanics of rock fracturing process: A numerical study. *Acta Geotech.* **2022**, *17*, 2799–2824. [CrossRef]
49. New Method for Evaluating Surface Roughness Parameters Acquired by Laser Scanning—Scientific Reports. Available online: https://www.nature.com/articles/s41598-019-51545-7 (accessed on 28 January 2024).
50. Bulaha, N.; Rudzitis, J. Calculation Possibilities of 3D Parameters for Surfaces with Irregular Roughness. *Latv. J. Phys. Tech. Sci.* **2018**, *55*, 70–79. [CrossRef]
51. Kumar, B. AFM studies on surface morphology, topography and texture of nanostructured zinc aluminum oxide thin films. *Dig. J. Nanomater. Biostructures* **2012**, *7*, 1881–1889.
52. Zhang, W.; Yamashita, S.; Kumazawa, T.; Ozeki, F.; Hyuga, H.; Kita, H. Influence of surface roughness parameters and surface morphology on friction performance of ceramics. *J. Ceram. Soc. Jpn.* **2019**, *127*, 837–842. [CrossRef]
53. Edachery, V.; Swamybabu, V.; Adarsh, D.; Kailas, S. Influence of surface roughness frequencies and roughness parameters on lubricant wettability transitions in micro-nano scale hierarchical surfaces. *Tribol. Int.* **2022**, *165*, 107316. [CrossRef]
54. Sinkhonde, D. Employing spatial, hybrid and amplitude roughness parameters for unveiling the surface roughness features of mineral and organic admixtures. *Heliyon* **2023**, *9*, e20539. [CrossRef] [PubMed]
55. Pearlstine, L.; Portier, K.M.; Smith, S.E. Textural discrimination of an invasive plant, Schinus terebinthifolius, from low altitude aerial digital imagery. *Photogramm. Eng. Remote Sens.* **2005**, *71*, 289–298. [CrossRef]
56. Haralick, R.M.; Shanmugam, K.; Dinstein, I. Textural Features for Image Classification. *IEEE Trans. Syst. Man Cybern.* **1973**, *SMC-3*, 610–621. [CrossRef]
57. Zhang, Y.; Sun, Q.; He, H.; Cao, L.; Zhang, W.; Wang, B. Pore characteristics and mechanical properties of sandstone under the influence of temperature. *Appl. Therm. Eng.* **2017**, *113*, 537–543. [CrossRef]
58. Zhu, T.; Jing, H.; Su, H.; Yin, Q.; Du, M.; Han, G. Physical and mechanical properties of sandstone containing a single fissure after exposure to high temperatures. *Int. J. Min. Sci. Technol.* **2016**, *26*, 319–325. [CrossRef]
59. Zhou, Z.; Cai, X.; Ma, D.; Cao, W.; Chen, L.; Zhou, J. Effects of water content on fracture and mechanical behavior of sandstone with a low clay mineral content. *Eng. Fract. Mech.* **2018**, *193*, 47–65. [CrossRef]
60. Jha, M.K.; Verma, A.K.; Gautam, P.K.; Negi, A. Study of mechanical properties of Vindhayan shaly rocks at elevated temperature. *J. Geol. Soc. India* **2017**, *90*, 267–272. [CrossRef]
61. Gautam, P.K.; Verma, A.K.; Jha, M.K.; Sharma, P.; Singh, T.N. Effect of high temperature on physical and mechanical properties of Jalore granite. *J. Appl. Geophys.* **2018**, *159*, 460–474. [CrossRef]
62. Hobbs, D.W. The tensile strength of rocks. *Int. J. Rock Mech. Min. Sci. Geomech. Abstr.* **1964**, *1*, 385–396. [CrossRef]
63. Diyuan, L.; Wong, L.N.Y. The Brazilian disc test for rock mechanics applications; review and new insights. *Rock Mech. Rock Eng.* **2013**, *46*, 269–287. [CrossRef]
64. Chen, Y.; Yin, T.; Ranjith, P.G.; Li, X.; Zhuang, D.; Wu, Y. Experimental investigation of a fissured rock with thermal storage potential subjected to descending amplitude low cycle impacts. *J. Energy Storage* **2023**, *72*, 108500. [CrossRef]
65. Nasseri, M.H.B.; Tatone, B.S.A.; Grasselli, G.; Young, R.P. Fracture Toughness and Fracture Roughness Interrelationship in Thermally treated Westerly Granite. *Pure Appl. Geophys.* **2009**, *166*, 801–822. [CrossRef]
66. Pijaudier-Cabot, G.; Bažant, Z. Nonlocal damage theory. *J. Eng. Mech.* **1987**, *113*, 1512–1533. [CrossRef]
67. Gdoutos, E. *Problems of Mixed Mode Crack Propagation*; Springer Science & Business Media: Berlin/Heidelberg, Germany, 2012.
68. Xie, H.; Ju, Y. Energy analysis and criteria for structural failure of rocks. *J. Rock Mech. Geotech. Eng.* **2009**, *1*, 11–20. [CrossRef]

Disclaimer/Publisher's Note: The statements, opinions and data contained in all publications are solely those of the individual author(s) and contributor(s) and not of MDPI and/or the editor(s). MDPI and/or the editor(s) disclaim responsibility for any injury to people or property resulting from any ideas, methods, instructions or products referred to in the content.